JGR Solid Earth

RESEARCH ARTICLE
10.1029/2021JB021905

Bayesian Estimation of Surface Strain Rates From Global Navigation Satellite System Measurements: Application to the Southwestern United States

C. Pagani[1], T. Bodin[1], M. Métois[1], and C. Lasserre[1]

[1]Univ Lyon, UCBL, ENSL, UJM, CNRS, LGL-TPE, F-69622, Villeurbanne, France

Key Points:

- A Bayesian interpolation scheme is applied to derive strain rates from discrete geodetic horizontal velocities
- Full probability density functions are provided for spatial derivatives of the 2D velocity field
- Consistent estimates of strain rates are obtained without underlying physical model nor ad hoc smoothing parameter

Supporting Information:

Supporting Information may be found in the online version of this article.

Correspondence to:

M. Métois,
marianne.metois@univ-lyon1.fr

Citation:

Pagani, C., Bodin, T., Métois, M., & Lasserre, C. (2021). Bayesian estimation of surface strain rates from Global Navigation Satellite System Measurements: Application to the Southwestern United States. *Journal of Geophysical Research: Solid Earth*, *126*, e2021JB021905. https://doi.org/10.1029/2021JB021905

Received 23 FEB 2021
Accepted 8 MAY 2021

Abstract Seismic hazard assessment in active fault zones can benefit of strain rate measurements derived from geodetic data. Producing a continuous strain rate map from discrete data is an inverse problem traditionally tackled with standard interpolation schemes. Most algorithms require user-defined regression parameters that determine the smoothness of the recovered velocity field and the amplitude of its spatial derivatives. This may lead to biases in the strain rates estimation which could eventually impact studies on earthquake hazard. Here we propose a transdimensional Bayesian method to estimate surface strain rates from Global Navigation Satellite System (GNSS) velocities. We parameterize the velocity field with a variable number of Delaunay triangles and use a reversible-jump Monte-Carlo Markov Chain algorithm to sample the probability distribution of surface velocities and spatial derivatives. The solution is a complete probability distribution function for each component of the strain rate field. We conduct synthetic tests and compare our approach to a standard b-spline interpolation scheme. Our method is more resilient to data errors and uneven data distribution, while providing uncertainties associated with recovered velocities and strain rates. We apply our method to the Southwestern United States, an extensively studied and monitored area and infer probabilistic strain rates along the main fault systems, including the San Andreas one, from the inversion of interseismic GNSS velocities. Our approach provides a full description of the strain rate tensor for zones where strain rates are highly contrasted, with no need to manually tune user-defined parameters. We recover sharp velocity gradients, without systematic artifacts.

Plain Language Summary Mapping the amplitude, type and direction of crustal deformation is of great help to detect active faults and ultimately estimate seismic hazard. However, systematic biases remain in the standard methods used to produce continuous maps of the strain rate components from discrete observations such as Global Navigation Satellite System (GNSS) long-term velocities. It is notably difficult to properly assert the uncertainties on the results. We propose a new method based on Bayesian inference to get the full probability distribution on the strain rate components. Proper uncertainties can therefore be attributed to these values that can be included correctly in seismic hazard assessment studies. We perform a synthetic test to compare this Bayesian method to a bicubic spline interpolation. We apply successfully this method to the California highly straining San Andreas system and neighboring Basin and Range.

1. Introduction

1.1. Surface Strain, Fault Behavior, and Space Geodesy

Imaging and quantifying the present-day lithospheric deformation is crucial to understanding how and where long-term tectonic loading is accommodated. Plate tectonics theory assumes that the relative motion of rigid lithospheric blocks is accommodated on a limited set of localized fault zones, where the lithosphere either deforms elastically during the interseismic period of the seismic cycle, or in a brittle way during the coseismic rupture (Isacks et al., 1968; Le Pichon, 1968; Morgan, 1968). In a simple elastic framework, the surface deformation generated by slip on a dislocation buried in an elastic half-space can be computed (e.g., Okada, 1985), as well as the surface deformation produced by full or partial locking of the buried fault using the "backslip" hypothesis (Savage, 1983). Analyzing the spatial patterns of surface deformation and their temporal variations around active faults can therefore help constraining the behavior of fault systems at each stage of the seismic cycle.

With the advent of space geodesy in the 1990s, and in particular the growing development of Global Navigation Satellite System (GNSS) networks in active fault zones, precise measurements of surface displacements made it possible to detect and model various processes of tectonic deformation, thus revolutionizing our understanding of fault seismic cycle (e.g., Bürgmann & Thatcher, 2013). The last decades have seen the number of geodetic observations of large earthquakes and interseismic strain along major faults increase significantly (e.g., Blewitt et al., 2018). Combined with an improved knowledge of the past seismic history of faults, such observations have highlighted a spatial correlation between portions of the seismogenic zone locked during the interseismic period and the coseismic rupture zones, while portions of faults aseismically slipping during the interseismic phase appeared as potential nucleation zones or barriers to earthquakes (e.g., Chlieh et al., 2008; Métois et al., 2016; Simons et al., 2011). This paved the way to provide plausible scenarios for future earthquakes based on the monitoring of interseismic surface strain rates (e.g., Avouac, 2015; Beauval et al., 2018; Kaneko et al., 2010).

If most of the deformation due to relative block motions is indeed taken up on well localized and mapped plate boundaries, the lithosphere can also deform in a more diffuse way on wider zones, in particular in and around collisional belts (e.g., Thatcher, 2009). Such diffuse deformation may be accommodated elastically by series of multiple active faults, or through other nonelastic processes within the lithosphere (Copley, 2008; D'Agostino et al., 2014; England & Molnar, 1997). In combination with geological, tectonic, and seismological data, geodetic measurements of surface deformation can then help to refine the degree of localization of the deformation over wide intracontinental areas, to identify active structures and constrain the style of the deformation, as well as the underlying mechanical processes.

Modern geodetic techniques now offer measurements of surface velocities with accuracy of the order of 1 mm/yr or below for the interseismic period. They each have their own contributions and specificities concerning the components of the ground motion that they capture, their resolution and their uncertainties, and appear to be very complementary. While horizontal and vertical motion can be measured by GNSS and optical image correlation, Interferometric Synthetic Aperture Radar (InSAR) only provide the projection of ground displacements in the line-of-sight (LOS) of the satellite. GNSS measurements remain spatially sparse, at discrete stations, but benefit from a temporal sampling up to $\simeq$1 Hz. Space geodesy based on optical and radar images, on the contrary, provide data at all satellite image pixels, with a temporal resolution dependent on the return time of the satellites. Finally, depending on the technique, uncertainties can be spatially and temporally correlated or not. Taking advantage of the large amount and diversity of geodetic data available today to constrain spatio-temporal variations of the strain rate field is a challenge for the community involved in seismic hazard studies.

1.2. The Strain Rate Tensor: Formulation, Assumptions, and Analysis

The variations of the strain rate field can be explored through the analysis of the velocity gradient $\nabla \boldsymbol{V} = \partial_i V_j$, its symmetrical part, and the strain rate tensor $\dot{\epsilon_{ij}} = \frac{1}{2}(\partial_i V_j + \partial_j V_i)$. Spotting regions with high strain rates may help identify active faults prone to high seismic hazard (e.g., Elliott et al., 2016). To this end, maps of the second invariant I_2 of $\dot{\epsilon}$ are built either at the local to regional scale (e.g., D'Agostino, 2014; Metois et al., 2015), or at the continental to global scale (e.g., Kreemer et al., 2014). Following Kreemer et al. (2003), Pérouse et al. (2012), D'Agostino (2014), and Metois et al. (2015), we define the second invariant of the horizontal strain rate tensor as:

$$I_2 = \sqrt{\dot{\epsilon}_{xx}^2 + \dot{\epsilon}_{yy}^2 + 2\dot{\epsilon}_{xy}^2}.$$

Note that most GNSS studies only consider the horizontal 2D tensor $\dot{\epsilon}$ (D'Agostino, 2014; Ward, 1998) or a partially 3D tensor (Mazzotti et al., 2011; Shen et al., 2015) for two main reasons: (a) the vertical component of the GNSS velocity is often associated with large uncertainties (Bennett & Hreinsdóttir, 2007), and (b) we have no access to the vertical derivative of the velocity components ($\partial_z V_x$, $\partial_z V_y$, $\partial_z V_z$). Joint GNSS-InSAR studies also remain limited to a 2D strain tensor analysis (e.g., Weiss et al., 2020). In this study, we only consider the horizontal velocity field and corresponding 2D strain rate tensor, while discussing in Section 6 the possibility to include V_z in future analysis.

Providing continuous maps of the different components or combinations of components of the horizontal strain rate tensor can help to understand the tectonic regime and style of deformation of a given area (e.g., Chousianitis et al., 2015; Kreemer et al., 2018; Metois et al., 2015; Pérouse et al., 2012). For example, the second invariant analysis gives clues on the variations of strain amount and localization across faults. The divergence of the velocity field $d = tr(\dot{\epsilon})$ highlights areas experiencing dilation or compression (a positive divergence stands for dilation while negative divergence is compression), while the horizontal vorticity defined as $\mathrm{rot}V = \partial_x V_y - \partial_y V_x$ allows the identification of nearly rigid blocks. The principal directions of the strain rate tensor may also be compared to directions of stress when the lithosphere is considered fully elastic. They are therefore often plotted against focal mechanisms or long-term stress orientations related to the geological setting (e.g., England et al., 2016; Mathey et al., 2020).

In the past decades, the geodetically derived strain rate tensor has also been used to derive the equivalent seismic energy stored as elastic deformation that could be released during earthquakes. In particular, Ward (1998) proposes to use the formula from Kostrov (1974) to calculate geodetic moment rates $\dot{M}_o^g$ from $\dot{\epsilon}$, in the case of a uniaxial strain. For a region of given area A, its geodetic moment rate is expressed as:

$$\dot{M}_o^g = 2\mu H_s A \dot{\epsilon}_{max}, \tag{1}$$

where μ is the rigidity modulus, H_s the seismogenic thickness, and $\dot{\epsilon}_{max}$ is the largest eigenvalue of the strain rate tensor $\dot{\epsilon}$. Comparing $\dot{M}_o^g$ to the released seismic energy based on historical and instrumental seismic catalogs provides information on the energy that remains to be released either seismically or aseismically (Angelica et al., 2013; D'Agostino, 2014; Mazzotti et al., 2011; Pancha et al., 2006; Ward, 1998).

1.3. Aim of the Study

As shown above, mapping continuous surface velocities together with their spatial derivatives and associated uncertainties can benefit a broad community. However, two main methodological limitations remain:

1. As in situ geodetic data provide spatially discrete and unevenly distributed information on the surface displacement rate, these data need to be interpolated in order to recover a continuous strain rate map. This also applies to InSAR data in case of low coherence. Such computing formally constitutes an inverse problem with a highly nonunique solution and a strong trade-off between model complexity and model constraints, that is, between the level of spatial resolution and the level of errors in the solution (Bodin, Sambridge, et al., 2012).
2. Uncertainties on the interpolated velocity field and their propagation onto the strain rate tensor components are often poorly estimated. These uncertainties are nonetheless required and crucial if we want geodetic estimates of the strain rates to integrate probabilistic seismic hazard assessment schemes (Beauval et al., 2018; Gerstenberger et al., 2020).

In this study, we propose to tackle these issues by applying a transdimensional Bayesian approach (Bodin, Salmon, et al., 2012) to the strain rate reconstruction problem. We first describe the different approaches used in the community to produce strain rate maps. We then present our inversion method and illustrate its potential benefits with synthetic tests. Because the San Andreas fault system has been extensively studied in the past and is particularly well instrumented, we build our synthetic tests from its simplified geometry and kinematics. We then propose a first application to real observations of a GNSS velocity field spanning the interseismic deformation across this fault system and the Southwestern United States. Finally, we discuss the main outcomes, advantages, and limitations of the proposed method. We show that we are able to provide a full probabilistic description of the strain rate tensor for zones where strain rates are highly contrasted, with no need to introduce user-defined parameters. Our method recovers sharp velocity gradients, therefore localizing strain, and distinguishing creeping from locked fault segments, without systematic biases.

2. Inverting for the Strain Rate Tensor: State of the Art

Since the first geodetic observations of ground movements by triangulation or leveling (e.g., Frank, 1966; Savage & Burford, 1970), several methods have been developed to infer surface strain rates from velocity fields. Today, they mainly use GNSS data (e.g., Kreemer et al., 2018; Masson et al., 2019; Shen et al., 1996; Vergnolle et al., 2007) and start to incorporate space geodetic data from InSAR and optical imagery (e.g., Barnhart et al., 2020; H. Wang et al., 2019). Some of these methods rely on geophysical models, such as elastic or visco-elastic block models with predefined active faults (e.g., McCaffrey et al., 2013; Parsons, 2006), to calculate surface velocity and strain rates. Others aim at deriving the strain rate tensor from surface observations alone, without any underlying physical model.

Among the "model-free" methods, two main approaches coexist in the literature. The most standard approach requires to first spatially interpolate local displacement rates measured at GNSS stations to build a continuous velocity field. The strain rate tensor is then simply obtained by taking the gradient of the interpolated velocity field. The interpolation (or 2D regression) is often conducted by fitting a spline function to the data (Beavan & Haines, 2001; Kreemer et al., 2003; Metois et al., 2015). The level of smoothing to interpolate the velocity field is usually arbitrarily defined by the user. For instance, in the *SPARSE* code developed in Beavan and Haines (2001), it is controlled by the interpolation grid spacing and the variance attributed to each grid cell (it can therefore be spatially variable). In the adjusted bi-cubic spline-in-tension method (referred to as the B-spline method in the following), a tension parameter must be chosen as well (Gan et al., 2007; Hackl et al., 2009; Smith & Wessel, 1990; Wessel & Becker, 2008; Wessel & Bercovici, 1998). This tension parameter is unique for the whole study area. In the case of unevenly spaced geodetic data, regions with the densest sampling may thus be over-smoothed and information may be lost. Other interpolation techniques have been proposed to limit this weakness. For instance, the velocity for each cell of the interpolation grid can be computed as the weighted average of velocities at neighboring GPS stations (Mazzotti et al., 2011). However, here again, the weighting function defining the smoothness of the solution needs to be defined by the user. The level of smoothness of the velocity field (i.e., the amplitude of its derivatives) directly determines the amplitude of the strain rate tensor. An arbitrarily fixed smoothing level is therefore a serious limitation to proper strain rate assessment. Finally, B-spline methods are based on a regularized optimization scheme, and thus do not offer any constraint on the uncertainties regarding the velocity field and the strain rate tensor (Aster et al., 2018), which is problematic in the context of hazard assessment.

In a second type of approach, geodetic strain rates are directly inverted from the GNSS data without the need for a velocity interpolation scheme (Shen et al., 1996; Spakman & Nyst, 2002; Ward, 1998). At each point on a regular geographical grid, assuming a constant strain rate field, a system of linear equations can relate the displacement and deformation at that point and GPS velocities at neighboring stations. The observed velocities at GPS stations can thus be inverted through a standard least-square scheme to recover the unknown deformation at any given point. This method offers more robust strain rate estimates as such rates are directly computed as weighted averages. It provides also a first-order estimate on strain uncertainties. Many studies have used such least-square inversion schemes for studying surface deformation in specific areas, as for instance Sagiya et al. (2000) in Japan, Chousianitis et al. (2015) in Greece, or Palano et al. (2018) in Iran. However, the parameter controlling the weighting decay with distance in the least-square inversion remains again arbitrarily chosen, and acts as a smoothing factor that affects the resulting solution. Efforts have been made to optimize the level of smoothing and to account for spatial variability of data density (Shen et al., 2007, 2015). In particular, Kreemer et al. (2018) propose an algorithm in which, for any given evaluation point, multiple least-square inversions from different stations triplets are conducted. The median strain rates over the ensemble of inverted ones are then provided at that point.

However, the standard techniques presented above remain sensitive to the GNSS network geometry (with unevenly spaced data in most cases), data outliers and ad hoc user parameters. This is now acknowledged as a major issue in the community, potentially leading to systematic artifacts that could be mis-interpreted as tectonic signals (e.g., Baxter et al., 2011; Hackl et al., 2009; Titus et al., 2011). In the Southwestern United States for instance, where seismic hazard is high, a wide range of methods have been applied in the last decades to recover the strain rate tensor (e.g., Hackl et al., 2009; Kreemer et al., 2012), with results that

may differ significantly (Sandwell et al., 2010). The remaining limitations in these methods are therefore preventing further integration of geodetic measurements in seismic assessment methods.

In an attempt to overcome such limitations, we propose a method based on Bayesian inference to invert discrete GNSS velocities for the continuous 2D surface displacement field and the associated velocity gradients and strain rate tensor. We follow from the work of Bodin, Salmon, et al. (2012) who proposed a transdimensional Bayesian surface reconstruction algorithm to estimate the Moho topography beneath Australia from a discrete set of local observations. In this approach, the reconstructed surface is parameterized with a mesh that self-adapts to the level of information in the data. This proves to be well suited for very heterogeneous data (spatially or in terms of data type and noise level). Choblet et al. (2014) used the same approach to reconstruct probabilistic maps of relative variations of coastal sea level from tide gauge records. The approach was also used by Husson et al. (2018) to reconstruct maps of vertical displacement rates from GPS measurements, and by Hawkins, Bodin, et al. (2019) and Hawkins, Husson, et al. (2019) to reconstruct maps of seal level rise by combining vertical GPS velocities, satellite altimetry, and tide gauge measurements. In this work, the reconstructed surface is defined by two parameters: the two components of the interseismic horizontal velocities measured at GNSS stations. Details of the method are presented in Section 4.

3. Tectonic Context of the Southwestern United States and GNSS Velocity Field

To test and illustrate the potential of our methodology, we need a data set that is heterogeneous in several aspects: heterogeneous in data coverage, with a combination of densely monitored and poorly sampled areas, heterogeneous in data quality with variable uncertainties, and spatially heterogeneous in the expected strain rate amplitude and style.

In all these regards, our study area, located in the Southwestern United States (31° to 43°N, 110° to 124°W, see Figure 1) is a good test case. The plate boundary between the Pacific and North American plates accommodates ≃5 cm/yr of relative right-lateral motion (Altamimi et al., 2017) partitioned over several active structures. The most famous one is the San Andreas strike-slip fault system that takes up to 78% of the relative plate motion (Bennett et al., 2003; Freymueller et al., 1999), the remaining motion being accommodated on a set of distributed active faults further inland. Eastward, the Sierra Nevada, and Central Valley behave as a nearly rigid microplate that moves 11.4 mm/yr Northwestward relative to the stable North American plate (Bennett et al., 2003; Pérouse & Wernicke, 2017). This microplate is bounded to the East by the Walker Lane and East California Shear Zone where right-lateral shearing is dominant, with a small amount of extension, and that hosted significant historical earthquakes (Bennett et al., 2003; Niemi et al., 2004; Wesnousky et al., 2012). The Garlock fault zone, near which the recent Ridgecrest sequence (July 2019, Mw max 7.1 [e.g., K. Wang & Bürgmann, 2020]) occurred, is a SW-NE left-lateral strike-slip structure perpendicular to the San Andreas and East California Shear Zone (Peltzer et al., 2001). The large Basin and Range province farther east extends up to the Wasatch mountain belt and is characterized by a series of normal faults accommodating on the order of 3 mm/yr of the relative plate motion (e.g., Niemi et al., 2004). The Wasatch fault zone, marking the boundary between the Basin and Range and the Colorado stable plateau, is the easternmost active structure of the plate boundary zone and is extending at low rates (1–2 mm/yr) that may allow for Mw 7 earthquakes with large recurrence time (Machette et al., 1991; Niemi et al., 2004; Pérouse & Wernicke, 2017).

This complex plate boundary area is one of the best studied fault zones on Earth and geodetic measurements have been conducted there since 1923 (date of the first leveling studies in the Parkfield area) and more extensively since the 1980s (e.g., Murray & Langbein, 2006; Snay et al., 1983). Since then, modern GNSS networks have been installed to monitor the ongoing surface deformation, for instance in the framework of the PBO (Herring et al., 2016), NEARNET/MAGNET (Blewitt et al., 2009), or SCIGN (Hudnut et al., 2001) initiatives. The observed deformation is due to a wide variety of physical phenomena: eulerian plate or microplate motions (Altamimi et al., 2016), interseismic loading on active faults (e.g., McCaffrey, 2005; Peltzer et al., 2001), coseismic and postseismic deformation due to relatively moderate but destructive earthquakes (e.g., Milliner & Donnellan, 2020; Murray & Langbein, 2006; Shen et al., 1994), volcanic inflation and deflation of the Long Valley caldera (e.g., Hammond et al., 2019; Marshall et al., 1997), and hydrological de-

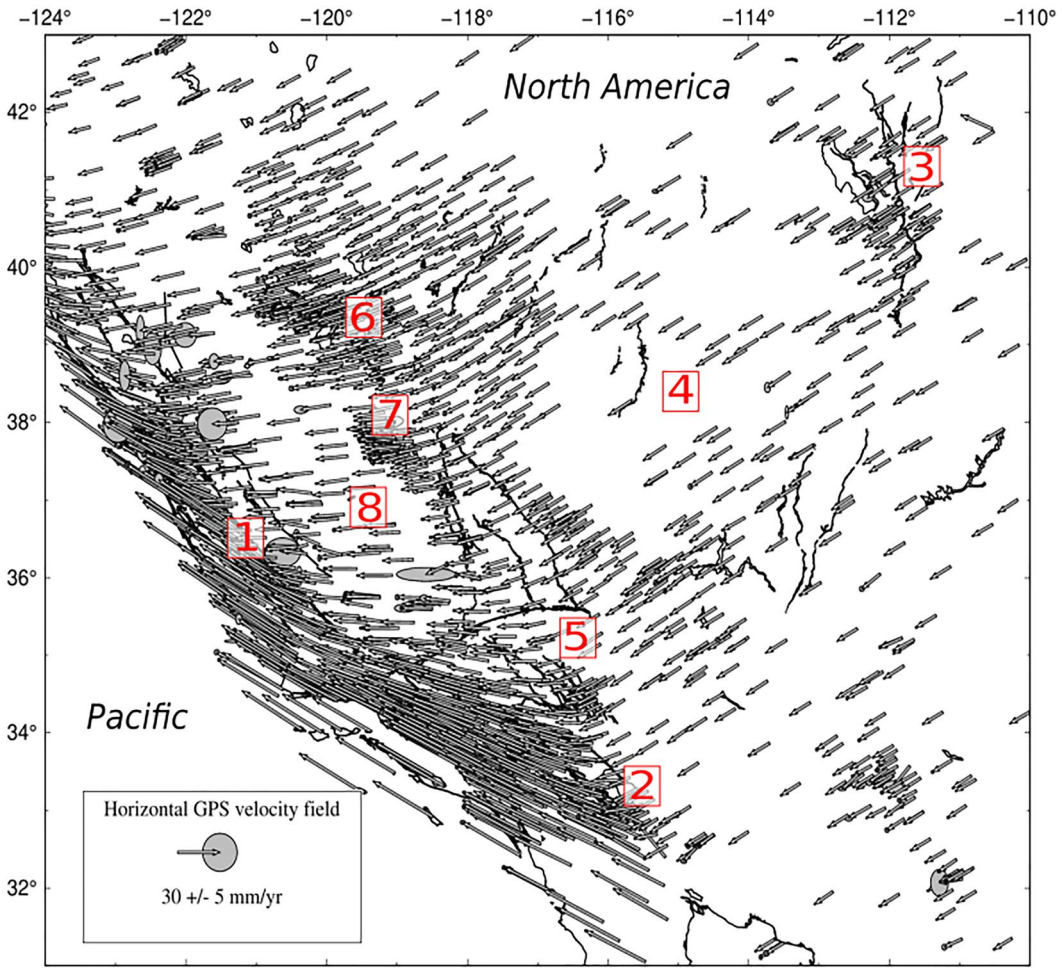

Figure 1. Horizontal GPS velocities from the Median Interannual Difference Adjusted for Skewness (MIDAS) data set in IGS14 reference frame in the Southwestern United States (this study area). Ellipses represent the uncertainties at 95% level. Black lines: active faults (Quaternary Fault and Fold Database, 2019). Note that the density of Global Navigation Satellite System stations is highly variable and higher near the San Andreas fault system. Key features of this plate boundary zone are labeled: 1—Monarch Peek creeping section (Central section) of the main San Andreas fault, 2—Salton Sea Lake zone, 3—Wasatch mountains fault zone, 4—Basin and Range province, 5—East California Shear Zone, 6—Walker Lane, 7—Long Valley Caldera, 8—Central Valley and Sierra Nevada.

pletion or infill of aquifers in particular in the Central Valley (Amos et al., 2014; Chaussard et al., 2017) or elsewhere (Silverii et al., 2020).

To represent the current deformation in Southwestern United States, we choose here to use the Median Interannual Difference Adjusted for Skewness (MIDAS) velocity field that compiles long-term velocities derived from GNSS daily times-series. It is provided by the Nevada Geodetic Laboratory (Blewitt et al., 2016, 2018). In our study area, the MIDAS data set, downloaded on February 2020 (see corresponding velocity file in Table S1), provides velocities for 2,441 stations with at least 4 years of recording from different local networks (PBO, MAGNET, SCIGN, see Figure 1). The velocities are calculated for the 1994–2020 time-span in the IGS14 reference frame.

In the densest parts of the velocity field, in particular near the San Andreas fault or in the Long Valley Caldera, baselines between stations are around 10 km (even shorter near some large city centers), while they reach more than 250 km in the less densely instrumented areas within the Basin and Range (Figure 1).

The MIDAS algorithm computes velocities for each individual time series as the median of the linear trends obtained between two dates separated by approximately 1 year (Blewitt et al., 2016). As a result, MIDAS

estimated velocities should be less affected by seasonality than when using classical regressions, and give robust estimates for surface average velocities (Hammond et al., 2016), except where nonlinear deformation, such as postseismic deformation or multi-annual hydrological loading, occurs. These types of deformation must be present in our data. Several major earthquakes occurred during the time period considered in the study area (notably the 1994 Northridge, 1999 Hector Mine, 2004 Parkfield, 2010 El Mayor-Cucapah, and 2019 Ridgecrest earthquakes). There is also evidence that multi-annual hydrological variation affects horizontal motion to some extent (e.g., Kim et al., 2021). However, we assume that the data set mostly captures the interseismic deformation in the area and we take into account the existence of nonlinear deformation effects by increasing the uncertainties on the MIDAS velocities. We remove only four stations from our data set, either because their velocities were computed on a too short time-span (lower than 1 year of continuous recording) or because their velocities were larger than 150 mm/yr on at least one component. In our study area, average uncertainties are of 0.31, 0.28, and 0.81 mm/yr on the East, North, and Up components, respectively. The uncertainties estimated by the MIDAS algorithm may be considered slightly overestimated compared to those obtained with usual techniques for long and clean time series (Mazzotti et al., 2020). However, because we chose to use on purpose the raw MIDAS interseismic velocity field provided online, without very restrictive quality criterion (see above), our data set may still include velocities that are not fully consistent with the long-term interseismic trends (when calculated on a too short time period or in cases of large data gaps for instance). To take into account this remaining heterogeneity in the data set, we thus chose to increase the MIDAS uncertainties by 10%. In the Bayesian inversion carried out in this study, we assume that errors affecting the velocities are Gaussian, uncorrelated between different stations and independent on each horizontal component. This is a strong first-order hypothesis. Indeed, the structure of noise on a single GPS station is usually considered to be composite, both white and flicker (Santamaría-Gómez et al., 2011; Williams et al., 2004), and spatially correlated noise has been identified on regional to global scale (also called common-mode error, see Benoist et al., 2020; Dong et al., 2006; Wdowinski et al., 1997). This hypothesis and its implications will be discussed further in Section 6.

To assess the behavior and the performances of our algorithm, we first create a realistic synthetic set of velocity measurements that mimics the real MIDAS velocity field described above. We compute a theoretical (target) velocity field, and sample it at each GNSS station used in MIDAS (see Section 5.1 for details on the synthetic model used). We then add random Gaussian errors to each measurement with a variance as given by MIDAS uncertainties. The resulting data set is inverted using our Bayesian algorithm and the results are compared with those obtained with a bi-cubic spline-in-tension interpolation method. In a second step, we apply the inversion scheme to the real MIDAS velocity field described above. Both data sets share the exact same characteristics and can be considered as an ensemble of displacement rates measured at n GNSS stations that can be formally described by the vector:

$$\mathbf{d_{obs}} = \begin{bmatrix} (V_{x_1}, V_{y_1}), \\ \dots, \\ (V_{x_n}, V_{y_n}) \end{bmatrix}$$

where (V_{x_i}, V_{y_i}) define the observed ground velocities for the ith of our n GNSS stations used as an input. Similarly, uncertainties associated with these observations are given by a vector

$$\boldsymbol{\sigma}_{\mathbf{obs}} = \begin{bmatrix} (\sigma_{x_1}, \sigma_{y_1}), \\ \dots, \\ (\sigma_{x_n}, \sigma_{y_n}) \end{bmatrix}$$

4. Method: Inverting for the Geodetic Strain Rate

4.1. Parameterizing the Velocity Field

To parameterize the continuous horizontal velocity field at the surface, we use a set of nodes scattered on the surface as represented in red in Figure 2. A horizontal velocity vector is assigned to each node. Note that nodes are independent of the location of the GNSS stations: their number, position, and velocity value

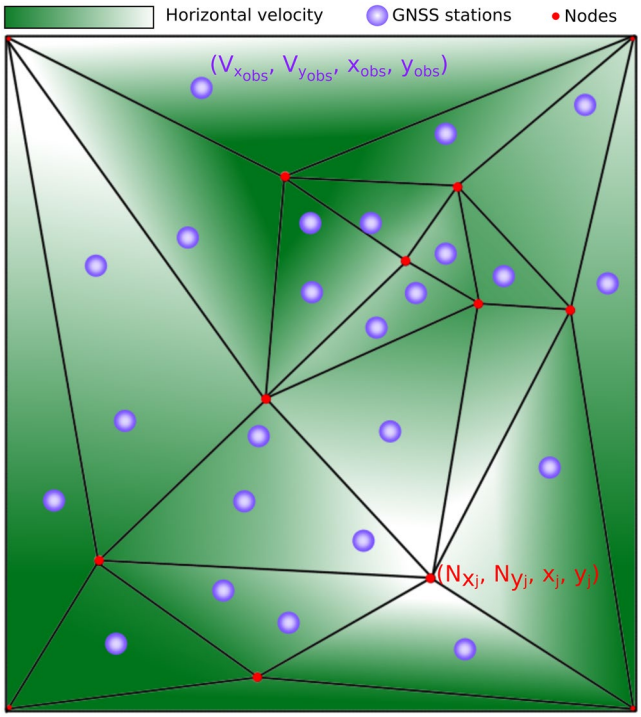

Figure 2. Example of surface meshing using Delaunay triangulation. Each node (in red) is assigned an horizontal velocity and the full velocity field (green gradient) can be obtained using a first-order linear interpolation between the vertices on each triangle. Vertices can be added, suppressed, or displaced during the algorithm, and their values can be modified. They are distinct from fixed Global Navigation Satellite System stations (in purple) where data are available.

are unknown parameters to be inverted for. They can be freely modified during the inversion. This surface parametrization is given by the vector:

$$\mathbf{m} = \Big[k, \quad (N_{x_1}, N_{y_1}, x_1, y_1), \ldots, (N_{x_k}, N_{y_k}, x_k, y_k)\Big]$$

where k is the number of nodes, and $(N_{x_j}, N_{y_j}, x_j, y_j)$ define the horizontal velocities and position for the jth node of the parametrization.

A continuous planar surface can be constructed from the vector **m**. The nodes are used to partition the plane into Delaunay triangles, so that no node is inside the circumcircle of any triangle. The velocity field within a triangle is then defined by a linear interpolation between the velocities assigned at each node defining the triangle. Within each triangle, the velocity field is a linear function of space, and the gradient (which is constant within the triangle) can be obtained from the node velocities through an analytical expression.

Delaunay triangulation schemes have previously been used to compute geodetic strain rates (Kreemer et al., 2018). In these techniques, the vertices are usually fixed, for example at the location of GNSS stations (Cai et al., 2008; Farolfi & Del Ventisette, 2017). In contrast, we propose here an evolutive triangulation: the nodes' location and velocity are the unknown of the inversion and will adapt to the level of information provided by the data. Higher concentration of nodes are mostly linked to deformation gradients rather than GPS data location, as can be seen in Figure S4.

Additional nodes are added at the four corners of the area of interest to insure that every point in this area is within the convex hull of the Delaunay triangulation.

4.2. Bayesian Inference

The solution **m** of our regression problem is clearly nonunique, and a Bayesian approach can be used to represent the solution in probabilistic terms (Tarantola, 2005). In a Bayesian framework, the solution to the inverse problem is the *a posteriori* probability density function (PDF), that is the probability of the model parameters **m** given the observed data $\mathbf{d}_{\mathbf{obs}}$. It can be written through Baye's theorem:

$$p(\mathbf{m} \mid \mathbf{d}_{\mathbf{obs}}) = \frac{p(\mathbf{m})p(\mathbf{d}_{\mathbf{obs}} \mid \mathbf{m})}{p(\mathbf{d}_{\mathbf{obs}})} \tag{2}$$

where $p(\mathbf{m})$ is the *a priori* probability distribution on the model (or prior), which represents our knowledge about the model before observing the data. In this work, we assume minimal prior knowledge, and use a uniform prior distribution within a reasonable range for each parameter. $p(\mathbf{d}_{\mathbf{obs}})$ is the evidence and can be ignored here as it is constant and does not depend on **m**.

The term $p(\mathbf{d}_{\mathbf{obs}}|\mathbf{m})$ is the likelihood distribution. It represents the probability of observing the data given the model and the distribution of data errors. Assuming that data errors are normally distributed with standard deviations given by $\boldsymbol{\sigma}_{\mathbf{obs}}$, the likelihood can be related to a L_2 misfit function, and expressed as:

Algorithm 1. rj-MCMC main loop

Start with an initial model described by a set of vertices $\mathbf{m}(N_{x_i}, N_{y_i}, x_i, y_i)$, obtained by randomly selecting a subset of the data and adding a random perturbation on position and velocity to each node.

for $i = 1, N_{\text{samples}}$ **do**

1: Propose a new model $\mathbf{m}$ by randomly perturbing the current model. Choose one of the following perturbation at random:

- Birth of a node on a random point of the surface.
- Death of a node.
- Change the horizontal velocity of a node.
- Displacement of a node.

2: Calculate the *a posteriori* probability of the perturbed model $p(\mathbf{m}'|\mathbf{d}_{\mathbf{obs}}|)$

3: Randomly accept the new model with probability $\alpha(\mathbf{m}' \mid \mathbf{m}) = f\left(\frac{p(\mathbf{m}' \mid \mathbf{d}_{\mathbf{obs}})}{p(\mathbf{m} \mid \mathbf{d}_{\mathbf{obs}})}\right)$ where $f(.)$ is a function defined in Bodin and Sambridge (2009).

4: If accepted, $\mathbf{m} \leftarrow \mathbf{m}'$. Else, $\mathbf{m} \leftarrow \mathbf{m}$.

5: Compute the velocity field $S(\mathbf{m})$ predicted for the model, and keep it in the ensemble solution. For each point of the map (i.e., on an underlying small grid as defined in Section 4.4), calculate the velocity field at the point, its spatial derivatives, the strain rate tensor, and any quantity of interest (second invariant, divergence, vorticity, ...). Store these values for the final distribution.

end for

$$p(\mathbf{d}_{\mathbf{obs}} \mid \mathbf{m}) \propto exp\left(-\sum_{i\in[1,n]}\left(\frac{\left(V_{x_i} - S_{x_i}(\mathbf{m})\right)^2}{2\sigma_{x_i}^2} + \frac{\left(V_{y_i} - S_{y_i}(\mathbf{m})\right)^2}{2\sigma_{y_i}^2}\right)\right), \tag{3}$$

where $S_{x_i}(\mathbf{m})$ and $S_{y_i}(\mathbf{m})$ stand for the components of the surface velocity predicted by the model $\mathbf{m}$ at the position of data points $[d_{x_i}, d_{y_i}]$. These values are compared with the observed velocities V_{x_i} and V_{y_i} at the same positions, the differences being weighted by the corresponding uncertainties on the velocities $(\sigma_{x_i}, \sigma_{y_i})$.

4.3. Sampling Models From the Posterior Distribution

We use a Markov chain Monte-Carlo (McMC) scheme to generate a large ensemble of models which distribution asymptotically converges to the *a posteriori* PDF. Here we use the reversible-jump McMC algorithm (Green, 1995, 2003) which is a generalization of the Metropolis-Hasting algorithm (Hastings, 1970; Metropolis et al., 1953) to the case where the number of parameters is variable.

This algorithm randomly explores the model space by generating a chain of models. The starting model is obtained by randomly selecting a subset of the data, creating a node for each GNSS station selected this way, and adding a perturbation to the node (in position and velocity). At each step, the current model is perturbed to produce a new proposed model. Then, the *a posteriori* probability of the current and proposed model are compared, and the new model is either accepted in the chain or rejected according to an acceptance rule depending on the ratio of posterior values. A pseudocode for the algorithm is given in table Algorithm 1 below. For a general description of McMC sampling, see Geyer (1992), Brooks et al. (2011), and Sambridge and Mosegaard (2002). For specific applications to transdimensional geophysical problems where the number of parameter is variable, see Bodin and Sambridge (2009), Bodin, Sambridge, et al. (2012), and Sambridge et al. (2013).

As the number of iterations in the Markov chain increases, the values of sampled parameters (e.g., the number of nodes) progressively converge toward a statistically stationary distribution which approximates the posterior distribution.

4.4. Extracting Relevant Information From the Ensemble Solution

It is important to note that the solution to our problem is not a single Delaunay velocity model that minimizes a misfit function. A model with zero misfit could be easily obtained by placing a Delaunay node at each GNSS station. However, such a model would be strongly unrealistic, as it would fit data errors, and depict a constant velocity gradient in each triangle, with sharp and discontinuous changes in strain rate at the triangle edges.

Instead, the solution of a Bayesian inverse problem is rather the entire *a posteriori* probability distribution (PDF), that is, an ensemble of velocity models with varying number of Delaunay cells. To appraise this distribution, we define an underlying grid (which can be as fine as needed for visualization), and store at each pixel of the grid the full distribution of all parameters of interest, such as velocity components, spatial derivatives, divergence, vorticity, I_2, or any other combination of the strain tensor components. By combining the information from several tens of thousands of models, we therefore obtain at each pixel of the map the entire probability distribution on any desired parameter.

For visualization, we exhibit 2D maps of statistical indicators for the parameter of interest: the representation of the posterior PDF is, at each point of the map, the average, the median value or the mode of maximum probability from all sampled models on that point. As an example, the mean vorticity map obtained for the synthetic test case presented in Section 5.1 is shown in Figure 3. In this way, a large number of models with different Delaunay parametrizations are stacked together. In a single model, the vorticity is constant over each triangle (top-left panel in Figure 3). But the continuous mean model contains features common to the entire family of models and considerably more information than any single Delaunay model.

Finally, it is important to insure that the algorithm has reasonably converged. A great number of models (typically between 10^4 and 10^5) are required to obtain an accurate depiction of the complete *a posteriori* probability distribution function. The influence of the number of models on the mean solution is shown in Figure 3, where the map of mean vorticity value is shown for different numbers of McMC iterations.

5. Results

5.1. Synthetic Tests on an Ideal San Andreas Fault

In order to assess the efficiency of our algorithm, we build a synthetic velocity field that results from the relative plate motion and interseismic loading on a simplified San Andreas fault. We use the TDEFNODE code developed by McCaffrey (2005) and based on Okada (1985)'s equations, and assume full locking of the fault (from 0 to 30 km depth) embedded in an elastic homogeneous half-space (Figures 4 and 5). The fault is designed as vertical and is forced to be purely strike-slip. The Pacific plate motion relative to the fixed North American plate is described by an ad hoc Euler pole (21.9°E, 14.2°N, 0.48/Myr), that generates an overall 5 cm/yr relative right-lateral motion.

We then extract the velocities at the locations of stations used in the MIDAS data set (see Section 3 and Blewitt et al., 2016), and add random Gaussian errors to each component with a variance given by the MIDAS uncertainties. We invert this synthetic data set to recover a continuous velocity field, its divergence, vorticity, and the second invariant I_2 of the strain rate tensor using two methods: our Bayesian algorithm presented above, and a standard bi-cubic spline-in-tension inversion method (see Figures 4 and 5). Our method could also be compared to other strain rate estimation schemes such as those proposed by Beavan and Haines (2001), Shen et al. (2015), or Kreemer et al. (2018). A large-scale comparison such as the one performed by Sandwell et al. (2010) is underway in France and will include this method in its results. In order to assess the quality of the inversion, we use the L_2 distance between maps of second invariant for the recovered model and those for the true synthetic model:

$$Distance = \sqrt{\frac{1}{n}\sum_{i=1}^{n}(I_2^{true} - I_2^{m})_i^2} \tag{4}$$

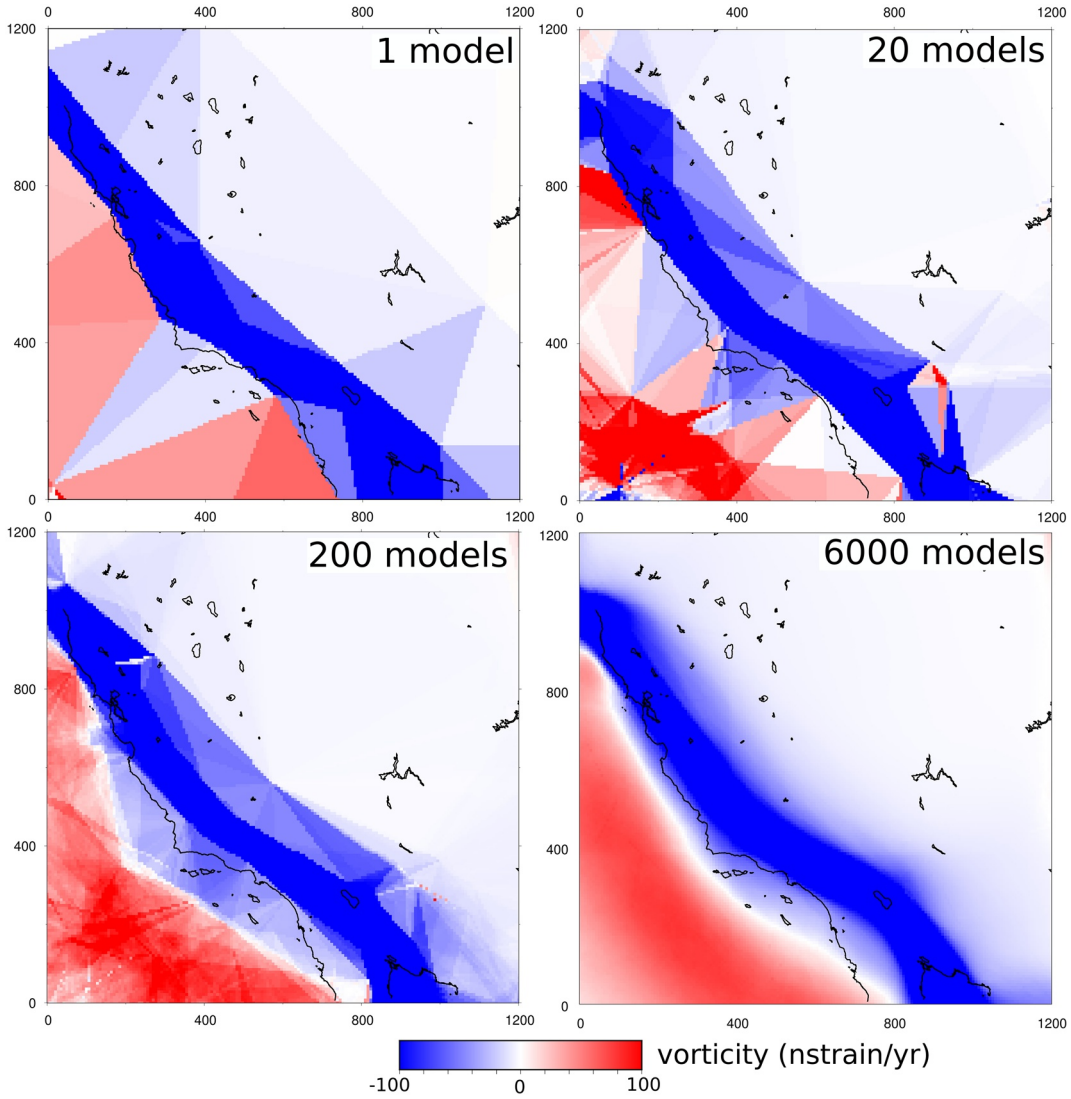

Figure 3. Convergence of the mean vorticity map. Convergence tests are performed on the synthetic velocity field built for our study area. Each panel shows the mean of the vorticity in the ensemble solution that is composed of either 1, 20, 200, or 6,000 models. As the number of sampled models increases (i.e., the number of steps in the random walk), the relevant characteristics of the vorticity field begin to appear while the triangle-shaped areas due to the Delaunay triangulation tend to fade away.

where I_2^{true} and I_2^m are the second invariant derived from the true synthetic model and the inverted velocity field, respectively, and n is the number of pixels in the maps. We choose to define the distance on I_2 rather than on the velocity components since inversion artifacts appear on the spatial derivatives of the velocity (Baxter et al., 2011; Hackl et al., 2009; Titus et al., 2011). This distance indicates the ability of a method to recover the original signal over the entire region for a given data distribution, though it does not reflect the level of data fit (measured only at stations).

To perform the B-spline interpolation, we use a minimum curvature approach, where the interpolated surface minimizes the level of data fit, while having continuous second derivatives and minimal total squared curvature (Smith & Wessel, 1990). We use the GMT *blockmean* and *surface* functions (Wessel et al., 2019), and calculate independently the velocity components V_{east} and V_{north} on each node of a predefined grid. In this procedure, the smoothness of the solution is determined by two parameters arbitrarily chosen by the user: the size of the grid and a tension parameter (see Smith & Wessel, 1990 for more details on the method). Those user-defined inputs are critical and should be carefully chosen. On Figures 4 and 5, the B-spline

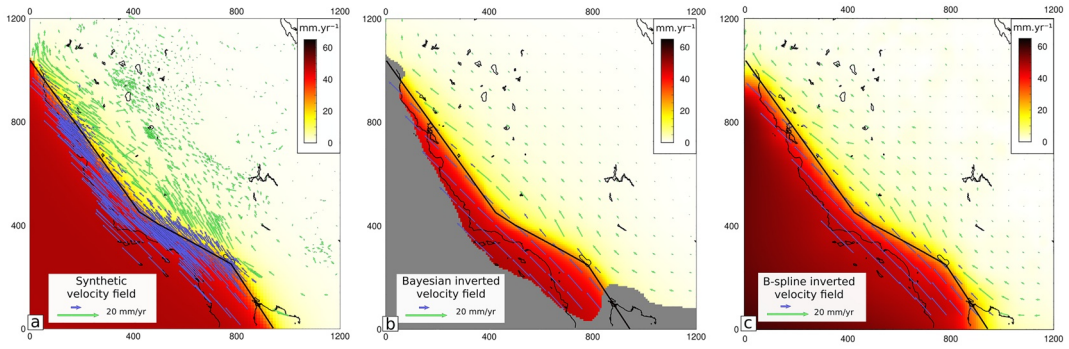

Figure 4. Synthetic tests for velocity field recovery on an idealized San Andreas fault. Black line: fault location. (a) The amplitude of the synthetic horizontal velocity is color coded. Blue and green arrows stands for the synthetic velocity data sampled at the position of the Global Navigation Satellite System stations from the real MIDAS velocity field, perturbed by the addition of a random Gaussian error. (b) Average velocity field obtained with our Bayesian scheme. Areas where the probability density function displays a standard deviation ≥3 mm/yr are masked. (c) Interpolated velocity field inverted with B-spline standard procedure.

solution that minimizes the distance to the true model (Equation 4) is obtained by manually adjusting the tension and grid parameters. Of course, in a real data case, this manual adjustment could not be done.

Figures 4 and 5 show the comparison of the mean of the posterior PDF obtained with our Bayesian scheme and that obtained with the B-spline interpolation, for the velocity field, vorticity, divergence, and second invariant. Overall, both inversion methods retrieve reasonably well the synthetic target with a fit to the true I_2 model of 37.6 and 39.5 nstrain/yr for the average of our Bayesian solution and B-spline best model, respectively. Though, major differences arise locally on spatial derivatives of the velocity field. The distributions for I_2, vorticity, and divergence obtained from B-spline inversion contain small wavelengths that are well known interpolation artifacts, mainly due to network geometry and data outliers (Baxter et al., 2011). Moreover, I_2 is systematically underestimated in the near field of the fault due to over-smoothing (by around 100 nstrain/yr), and the divergence map is particularly affected by small scale artifacts that may lead to incorrect interpretations. On the contrary, the average maps resulting from the Bayesian inversion are free from these small scale artifacts and recover well both the amplitude and spatial variations of deformation.

5.1.1. Noise Sensitivity

One of the main limitation of conventional approaches used to produce strain rate maps is their high sensitivity to noise. As shown in Figure 5, the Bayesian inversion appears significantly more resilient to errors than the B-spline method. The patchy aspect of the divergence map obtained from the B-spline interpolation could be reduced by using a higher level of smoothing but any significant signal in the near field of the fault would then be lost.

We test the influence of the level of noise added to the synthetic data set on both inversion techniques. Random errors are kept Gaussian and uncorrelated between stations. We test different synthetic data sets, progressively increasing their noise using a scaling factor varying between 0 and 3 on the errors given by the MIDAS uncertainties, and following the generation process described in Section 5.1. Because results from the B-spline interpolation highly depends on user-defined parameters, as mentioned above, we systematically test different smoothing values (i.e., grid steps) for each noise level with a constant tension. We compare in Figure 6 the results obtained for the B-spline and Bayesian methods. For the Bayesian inversion, we represent both the average and the median of the I_2 PDF.

As expected, the quality of both interpolations decreases with the level of noise. However, the Bayesian scheme performs better that the B-spline inversion, whatever the smoothing factor (i.e., grid step) considered. Figure 6 also illustrates well the sensitivity of the B-spline interpolation to the smoothing parameter (grid step): low smoothing produces data over-fitting and unstable results, whereas high smoothing causes information loss. Our Bayesian inversion scheme avoids having to arbitrarily choose the level of complexity in the reconstructed model (Bodin & Sambridge, 2009).

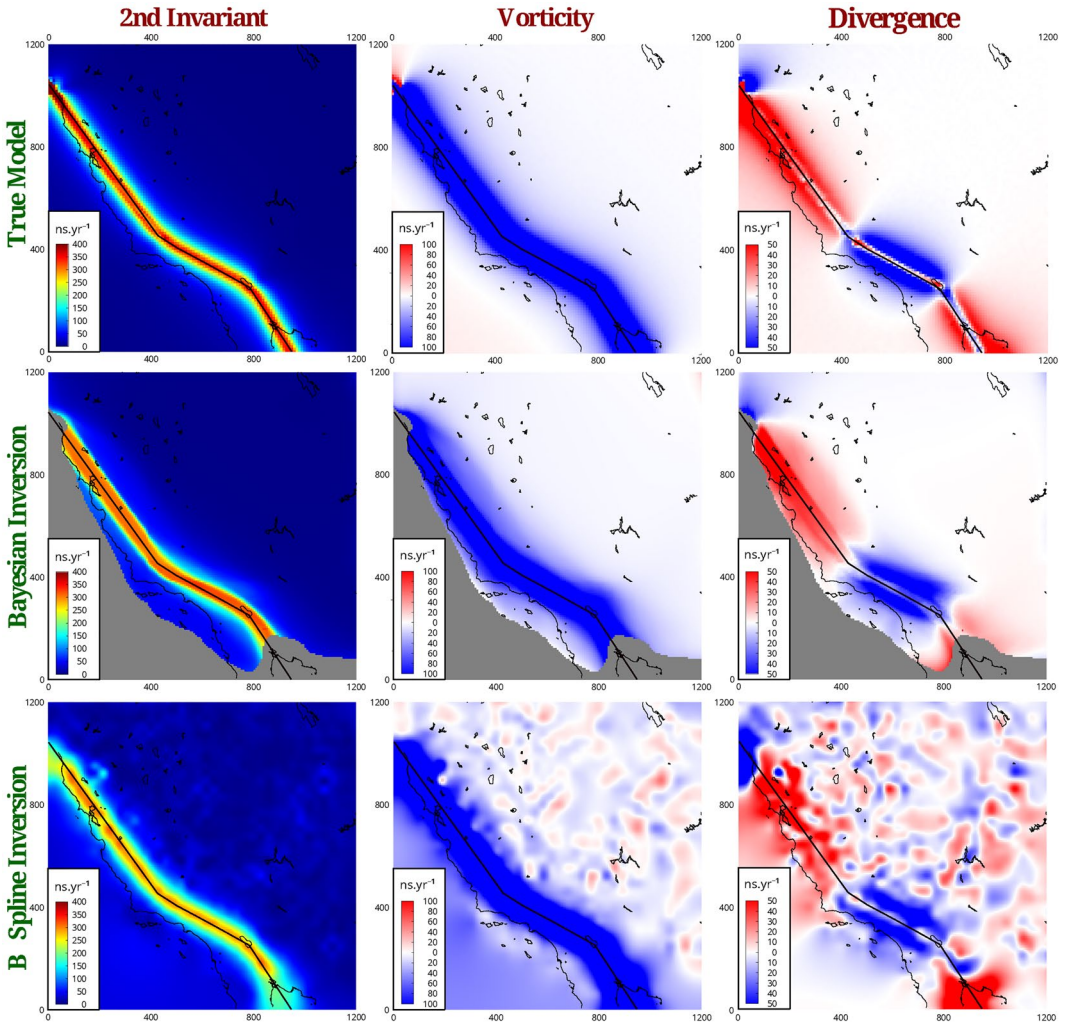

Figure 5. Strain rate tensor recovery from our synthetic test on an idealized San Andreas fault. Maps of the second invariant (left), vorticity (center), and divergence (right, compression is negative, dilation is positive) of the strain rate tensor are shown. The values expected from our synthetic model are shown on the upper panels ("true model"), together with results from our Bayesian inversion (average of the posterior distribution, middle), and from standard B-spline inversion (model obtained with optimal tension and grid parameters, lower panels). Black line: simplified San Andreas fault trace. Areas where the standard deviation of the horizontal velocity probability density function is higher than 3 mm/yr are masked since our Bayesian inversion is insufficiently constrained there (see Figure 4). Parameters of the B-spline inversion were chosen to minimize the distance to the true model on the second invariant (see Equation 4).

5.1.2. Visualizing and Interpreting the Posterior Solution

Obtaining a comprehensive estimate of the posterior uncertainties affecting the interpolated velocity field and its spatial derivatives can be challenging. One option is to consider at each geographical point the standard deviation of the posterior PDF for each inverted parameter (velocity, I_2, vorticity, divergence). We plot in Figure 7 this error map for the norm of the horizontal velocities. The standard deviation is the highest where data are scarse or missing: there, the solution is not constrained and the PDF is nearly flat. We chose to mask these unconstrained zones based on a threshold value fixed at 3 mm/yr (see gray areas in Figure 5 for instance). On the other hand, zones where the velocity field is well captured by the data set are characterized by low error values (≤0.5 mm/yr). Intermediate levels of errors are observed in areas with a strong velocity gradient, that is, in the very near field of the San Andreas fault in our synthetic model.

A careful inspection of the posterior distribution can be conducted on areas of interest to better interpret the results. A convenient way to do so is to plot the full distribution on chosen cross sections. In Figure 8,

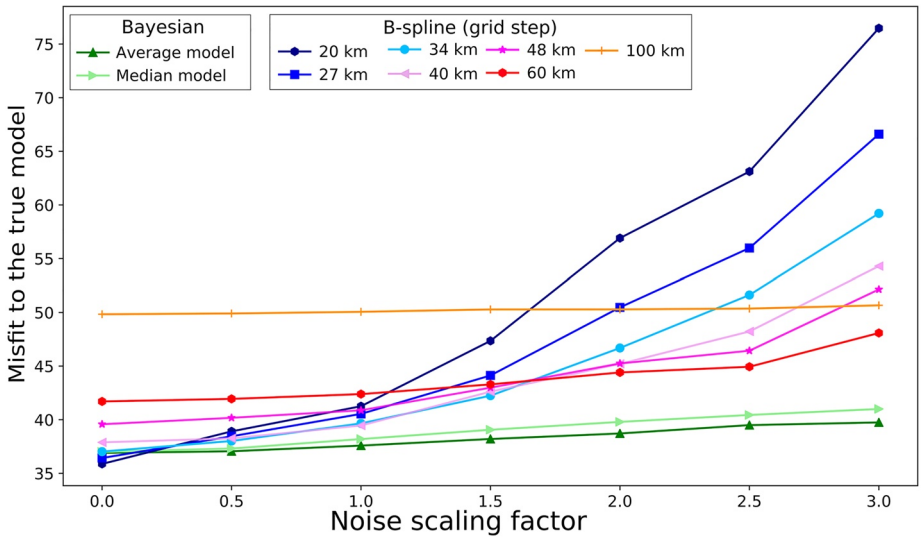

Figure 6. Distance to the true model calculated on the second invariant for the Bayesian inversion (based on the average model) and the B-spline method, for increasing level of data noise (see Equation 4). Different B-spline inversions with increasing grid steps, corresponding to an increased level of smoothing are presented.

we present the posterior distribution for both components of horizontal velocity (b and c), second invariant I_2 (d), divergence (e), and vorticity (f) along a 230-km-long profile roughly perpendicular (azimuth N55) to the southernmost section of the San Andreas fault (see Figure 8a). The normalized probability distribution is color coded for each pixel. The mean and 90% credible interval of the distribution are indicated as well as the result from the B-spline interpolation method and the true synthetic model. The posterior distributions for the velocity components are very narrow (<1.5 mm/yr wide), and centered on the true model. The distribution is wider for the derivatives because small oscillations in the velocity field can lead to substantial variations on the components of the strain rate tensor. The true model is enclosed in the 90% confidence interval and is in general well estimated by the mean of the distribution, except in the very near field of the fault, where deformation is strongly localized.

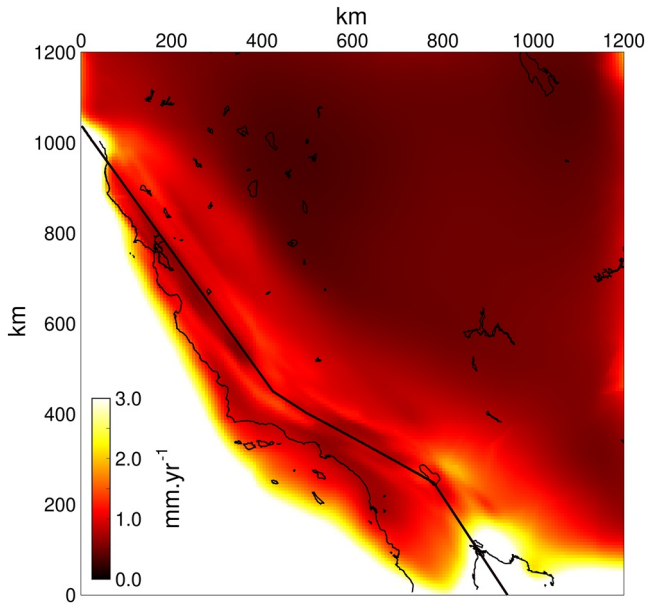

Figure 7. Standard deviation of the probability density function obtained for the norm of the horizontal velocity using our Bayesian method on synthetic noisy data set (noise factor of 1). The color scale is saturated for $\sigma \geq 3$ mm/yr, this threshold help masking the poorly constrained areas in Figures 4, 5 and 9. Areas of high velocity gradients are characterized by intermediate standard deviations, while zones with no or few data exhibit higher standard deviations (e.g., edges of the studied area). This statistic measure can be used as a proxy for the robustness of the result (see Figure 5).

Results from the B-spline interpolation often deviate significantly from the true model with misplaced or nonexistent oscillations, that are directly due to noisy data and that correspond to the small-wavelength patches seen in Figure 5. It is therefore difficult to conduct a proper interpretation of spatial derivatives of the velocity field obtained from direct interpolation schemes, especially since these artifacts resemble the signal that could be expected around active faults (Baxter et al., 2011; Hackl et al., 2009; Titus et al., 2011).

5.2. Bayesian Inversion of the MIDAS Data Set

We finally invert the real observations from the MIDAS data set (Blewitt et al., 2016) with associated uncertainties described in Section 3. We present in Figure 9 the map of posterior mean for I_2 and the divergence (see Figures S1–S3 in the supplementary materials for map of the vorticity, standard deviation, and velocity residuals). Figure 10 shows the full distribution plotted along two distinct profiles, perpendicular to the San Andreas fault, of the fault-parallel velocity component and second invariant

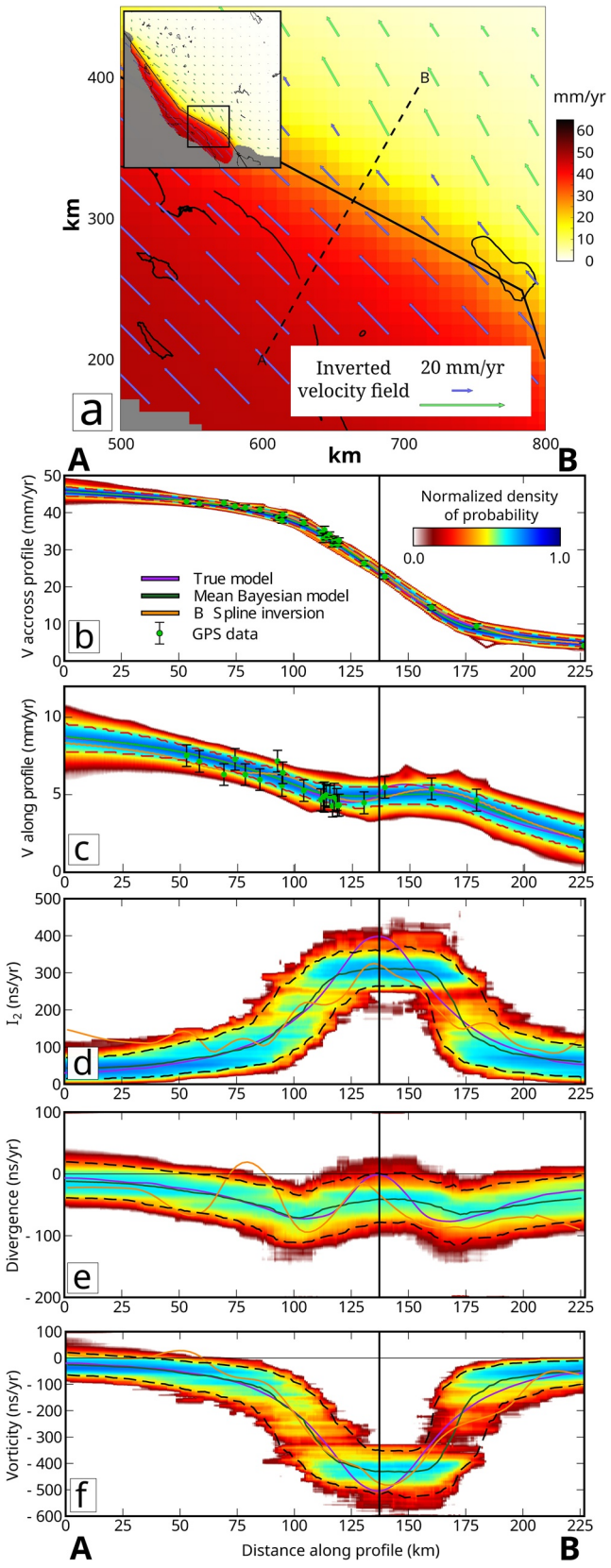
a
B
mm/yr
60
50
40
30
20
10
0
km
400
300
200
500
600
700
800
km
Inverted velocity field
20 mm/yr
A
B
b
V accross profile (mm/yr)
Normalized density of probability
0.0
1.0
True model
Mean Bayesian model
B Spline inversion
GPS data
c
V along profile (mm/yr)
d
I_2 (ns/yr)
e
Divergence (ns/yr)
f
Vorticity (ns/yr)
Distance along profile (km)
A
B

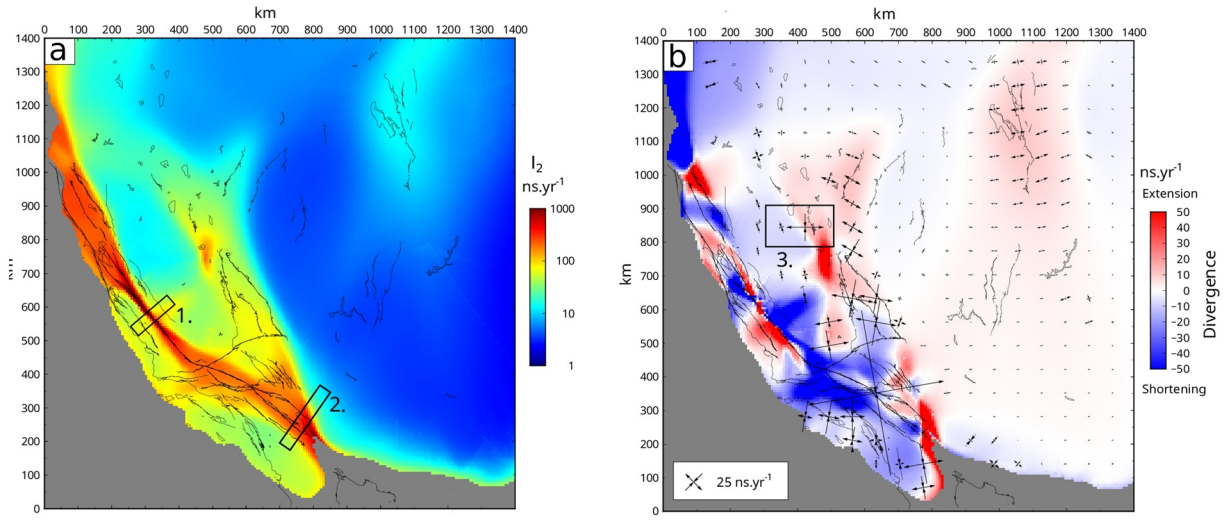

Figure 9. (a) Average of the *a posteriori* probability density function (PDF) of the second invariant of the strain rate tensor I_2 in nstrain/yr. The color scale is saturated for values above 1,000 nstrain/yr. Black lines: active faults from Quaternary Fault and Fold Database (2019). Box 1 and 2 stand for the chosen cross sections presented in Figure 10 for the creeping segment north of Parkfield (Monark peek segment) and Salton Sea Lake segments, respectively. (b) Same but for the divergence. Positive divergence stands for extension, negative for compression. Black arrows: mean of the principal directions of the strain rate tensor for an arbitrarily chosen set of points, scaled by their amplitude. Box 3 is the area represented in Figure 11.

I_2. These profiles in Figures 10a and 10b cross the creeping, Monarch Peek and locked, Salton Sea lake segments of the San Andreas fault, respectively.

The recovered map of second invariant is rather smooth, except in the near field of the San Andreas fault zone where high values of I_2 (higher than 1,000 nstrain/yr) are observed on relatively narrow zones around the main fault. In the Walker Lane, I_2 reaches intermediate values (~100 nstrain/yr) while it is lower than 10 nstrain/yr in the Basin and Range area with a slight increase over the Wasatch mountains.

The Salton sea lake segment (box 2 in Figures 9 and 10b) shows a 80 km wide zone of deformation around the fault. An extreme situation is observed along the Monarch Peek segment (box 1 in Figures 9 and 10a) where I_2 reaches values well above 1,000 nstrain/yr on a 15 km narrow zone around the main fault. Both zones are relatively well constrained by the data set since the posterior distribution of the velocity components is narrow all along the profile line, except in the very near field of the fault along the Monarch Peek segment. Distributions are wider for I_2 than for velocities, in particular when crossing the active faults. The average, median and maximum probabilities are plotted, together with the 90% confidence interval. Differences are small between the average and median in the velocity profiles (less than 1 mm/yr) and trends are very similar in I_2 cross section. Some significant variations arise when looking at the maximum probability mode that exhibits sharper transitions in particular in the Monarch Peek profile (Figure 10a).

The map showing the mean of the distribution for the divergence exhibits much more complex spatial variations (Figure 9b). Values range from −500 to 300 nstrain/yr, with extrema located in the vicinity of the San Andreas main fault zone (color scale is saturated in Figure 9b for clarity). Compression is dominant in the Garlock-San Andreas junction zone, while extension occurs at low rates in the Wasatch mountains in a nearly E-W direction. Slightly higher dilation rates are observed in the Walker Lane region (20–30 nstrain/yr) and in the Long Valley caldera (up to 200 nstrain/yr locally). Some localized extensional areas are also found in the vicinity of the main San Andreas fault zone in agreement with previously published dilatation

Figure 8. Slices of the entire probability density function (PDF) for different parameters along the cross section displayed on pannel a. The location of the fault is materialized by a vertical black line on the profiles. The horizontal axis represents the distance along the section and the vertical axis corresponds to the range of the prior, that is, the allowed range of values for the parameter. The color scale indicates the probability for the parameter on each point to take the corresponding value in the posterior. Profiles of the true model, the mean Bayesian model, and the B-spline inversion are superposed on the PDF. The black dotted line delimits the interval of 90% confidence. Profile stands for the PDF of the velocity along (b) and across profiles (c), of the second invariant (d), divergence (e) and vorticity (f) of the strain rate tensor.

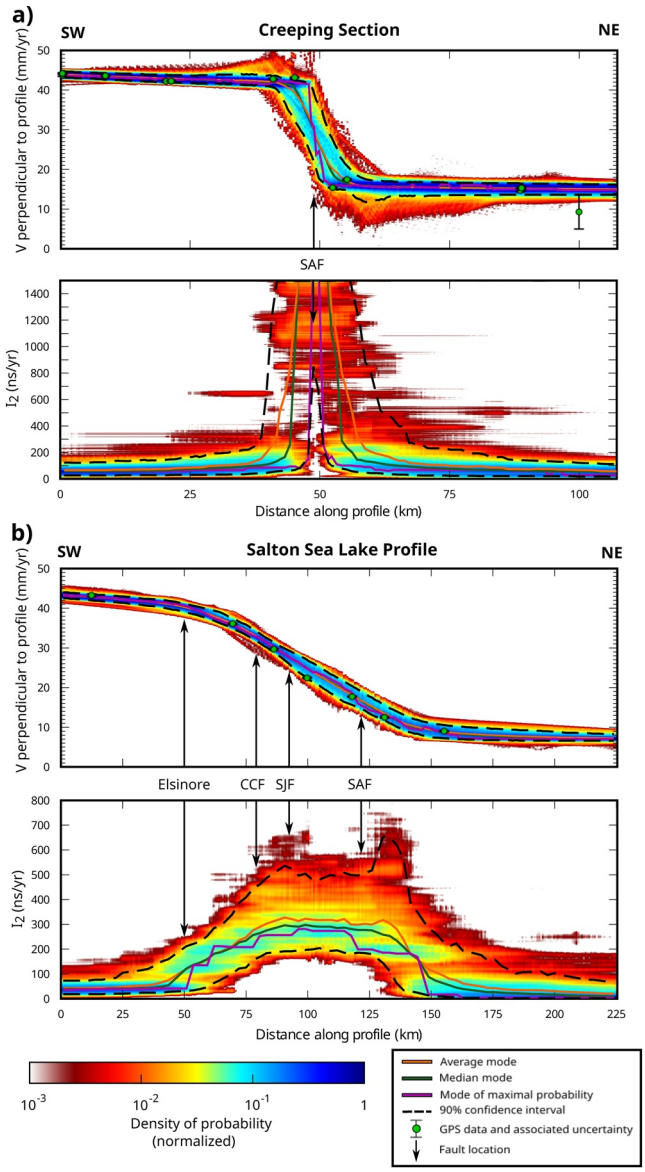

Figure 10. Variations of the profile-perpendicular velocity component (or fault-parallel velocity component, panel a) and I_2 (panel b) along two profiles shown in Figure 9. The full posterior probability (normalized) is plotted together with its average (orange line), median (green line), maximum (purple), and 90% of probability envelop (dashed black line). Black arrows stand for the main mapped faults (Fialko, 2006; Quaternary Fault and Fold Database, 2019): SAF: San Andreas fault, SJF: San Jacinto fault, CCF: Coyote Creek fault, and Elsinore fault.

maps (e.g., Kreemer & Hammond, 2007). However, similarly to the second invariant, the divergence in the vicinity of the creeping segment should be examined with extreme caution: at the position of the Monarch Peek segment, the distribution is widely spread out as the 90% confidence interval ranges from −850 to 420 ns/yr and display a rather homogeneous shape (Figure S5). Therefore the mean or median values are not representative of the distribution and should not be used for geophysical interpretations.

To further discuss the tectonic style in the area, we also compute the distribution for principal strain rate directions, and plot the mean directions in Figure 9b. Figure 11 shows a representation of the full distribution corresponding to box 3 in Figure 9b as rose diagrams. It provides a convenient way to jointly plot the principal strain rate direction, its amplitude (length of the histogram bin), style (compression is blue, extension is red), and the associated normalized probability (color coded, see Figure 11). Using such a representation, one can assess how well constrained is the strain rate tensor and whether the tectonic style is robustly defined: for instance, the dispersion is lower around the principal directions to the East (Walker Lane) than to the West (Sierra Nevada). In the Sierra (Figure 11, left), the windrose shows a large dispersion both in the direction of the principal strain and in their amplitude: while the maximum probability mode, represented by the directions in brightest red and blue, shows a dominant roughly N160 compression and a limited N70 extension, a few models, represented by the bars in lightest red and blue, propose a dominant N110 extension and a limited N20 compression, that is, a completely distinct tectonic regime. Such poorly constrained principal strain rate components should therefore be considered with extreme caution if used for tectonic interpretation.

6. Discussion

6.1. Advantages and Limits of the Bayesian Surface Reconstruction

As shown with synthetics tests, our method provides better strain rate estimates compared to conventional interpolation schemes, where the level of smoothing is manually adjusted by the user. In a transdimensional formulation, the number of parameters defining the surface is not fixed in advance, and the complexity of the solution (smoothness) naturally adapts to the level of information present in the data. A probabilistic solution also provides a full description of uncertainties for any parameter of interests (here, vorticity, divergence, etc.) by the PDF visualization either on one specific pixel, or in cross sections as presented in Figure 10. In the case of nearly Gaussian PDF, the standard deviation σ (Figure S1 for the inversion of the MIDAS data set) is a good estimate of the overall uncertainty on the inverted parameter. In particular, our approach can provide uncertainty estimates on the largest eigenvalue of the strain rate tensor, which is used in the Kostrov formulation for geodetic moment rate calculation (D'Agostino, 2014; Kostrov, 1974). Some PSHA techniques are also starting to integrate geodetic estimates of surface strain (Beauval et al., 2018). The full posterior distribution for principal directions, velocity derivatives, and strain rate invariants estimated with our approach could directly be included in logic trees.

However, our method is based on a Monte-Carlo sampling scheme where a large number of Delaunay models are tested against the data, and is therefore computationally intensive. Our final ensemble solution

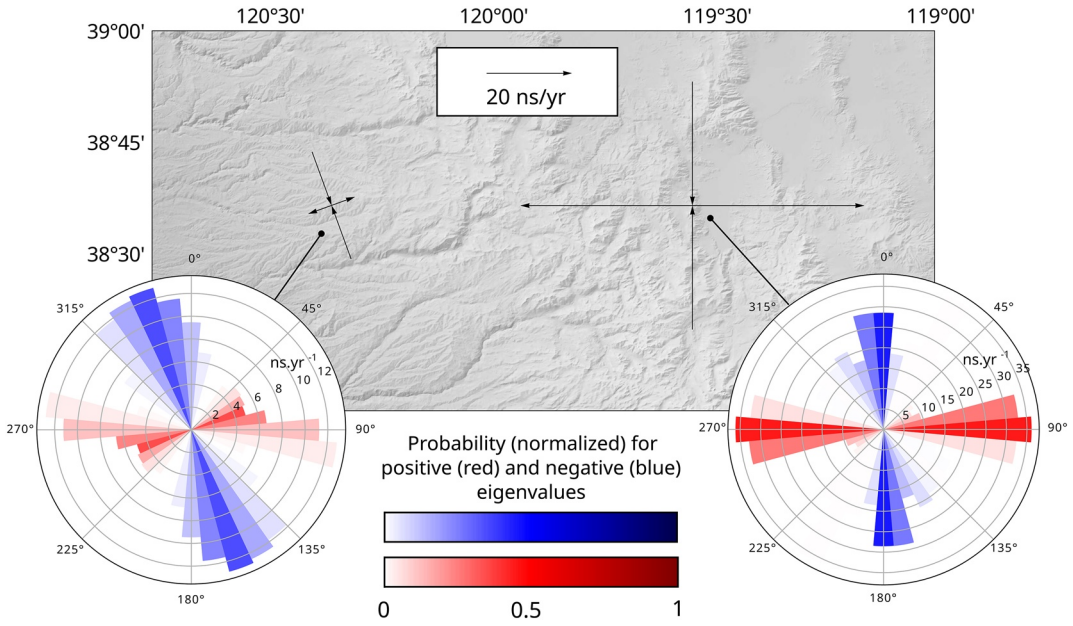

Figure 11. Zoom on Sierra Nevada (west) to Walker Lane (east) transition zone (zone 3 in Figure 9b). Black arrows stand for the average of the probability density function (PDF) for the principal components of the strain rate tensor. A more complete description of the PDF is proposed as windroses for both points: the amplitude (in nstrain/yr) and normalized probability (color coded) is represented for each 10° bin. Blue stands for compression, red for extension.

represented in Figure 9 is obtained after 84 h of calculation on 92 parallel processors, which is much larger than standard interpolation approaches.

We shall also acknowledge that a Bayesian formulation is entirely based on the mathematical model used to describe the statistics of data errors. In this study, we assume that the errors are Gaussian, and uncorrelated between different stations and between each horizontal component. A more accurate model could be used to account for the spatial correlation of errors in regional velocity fields, as well as for the correlation of errors between components (Benoist et al., 2020; Dong et al., 2006; Santamaría-Gómez et al., 2011; Wdowinski et al., 1997; Williams et al., 2004). This can be done by using a full covariance matrix of data errors in the likelihood function (Bodin, Sambridge, et al., 2012). A Bayesian scheme naturally propagates errors in the data toward errors in the posterior solution, and the form of the probabilistic solution also depends on the estimated amplitude of data uncertainties. If data errors are misestimated, posterior uncertainties will also be misestimated. In the case where data uncertainties are difficult to quantify, the total level of errors can be treated as an unknown parameter to be inverted for in a Hierarchical Bayes framework (Bodin, Salmon, et al., 2012; Gouveia & Scales, 1998). This hierarchical approach was successfully used in this study for synthetic tests: the level of noise added to the synthetic data was considered unknown in the inversion and was correctly recovered by the algorithm. However, when the hierarchical approach is used for the MIDAS data set, data uncertainties were clearly overestimated because of two effects: (a) the noise affecting observations is not Gaussian, and (b) observations are partially inconsistent from one station to another because of local effects unrelated to interseismic deformation. This led to important losses of structures, for example, in the Wasatch mountains fault area. Conversely, fixing the level of uncertainties to MIDAS uncertainties resulted in the addition of extra triangles needed to fit the data down to the level of observational noise, leading to artifacts due to incoherent stations. We decided to increase the noise by 10% as it was the smallest value for which we could get rid of said artifacts.

We shall also note that the method presented in this study has been implemented in Cartesian coordinates, that is, assuming the effect of Earth's sphericity is negligible. This assumption requires the use of a projection adapted to the region of interest, and remains valid as long as one concentrates on relatively small areas. In the present case, using a transverse Mercator projection, the deformation remains less than 1% up to 800 km from the reference meridian, which includes the entire region studied. However the code

should be adapted to spherical coordinates if to be applied to larger continental-scale regions (e.g., Haines & Holt, 1993; Kreemer et al., 2014, 2018; H. Wang et al., 2019).

6.2. From a Probabilistic Solution to Tectonic Interpretations

The method is applied to one of the most extensively studied area in terms of active tectonics: the San Andreas strike-slip fault system and the neighboring Basin and Range extensional area (see Section 3 and references therein). The maps of second invariant and divergence presented in Figure 9 agree with previous studies (e.g., Holt et al., 2000; Kreemer & Hammond, 2007; Kreemer et al., 2012; McCaffrey, 2005) which have been compared by Sandwell et al. (2010). We confirm that (a) transtension is dominant in the Walker Lane (Wesnousky et al., 2012), (b) the innermost Basin and Range (Central Great Basin) experiences very low strain rates and could therefore be considered as rigid (Bennett et al., 2003), and (c) 10 nstrain/yr of roughly E-W extension occurs in the Wasatch mountains (Niemi et al., 2004). Previous studies have argued whether or not the Sierra Nevada and Central Valley can be considered to behave as a rigid block (Bennett et al., 2003; Kreemer et al., 2014); our results tend to show that this area deforms internally and accommodates some amount of NNW-SSE directed compression ($I_2 \geq 10$ nstrain/yr).

In addition, our mean map of second invariant depicts very clear along-strike variations in the width of the highly straining area near the main fault of the San Andreas system, that are consistent with the along-strike segmentation of the fault. In particular, our results clearly highlight creep along the Monarch Peek segment (Ben-Zion et al., 1993; Jolivet et al., 2015; Rolandone et al., 2008), located in between locked fault sections northwest and southeast of it. To investigate further the ability of our method to capture along-strike segmentation without *a priori* information on the fault position, we plot the full PDF for I_2 and for fault-parallel velocities on two selected profile across Monarch Peek and Salton Sea segments (Figures 9 and 10). The surface velocity gradient across the fault (between 40 and 45 mm/yr depending on the considered segment) is accommodated on a 80 km wide zone around the Salton Sea segment while it is concentrated on a narrow 15 km wide zone around the Monarch Peek creeping segment. There, the expected velocity change should be even more abrupt (as seen from InSAR analysis for instance, Jolivet et al. 2015) but the GNSS network is not dense enough to capture changes over distances smaller than 15 km. However, interestingly, the mode of maximum probability exhibits such an abrupt change while the average and median of the PDF are smoother (Figure 10a). The second invariant I_2 along the creeping segment increases abruptly near the fault, starting around 10 km from it, well above 1,000 nstrain/yr.

In the Salton Sea Lake area, several faults are parallel to the main San Andreas fault and potentially active (Figure 10b). Identifying the amount of relative motion that is taken by each of these structures is still debated (Fialko, 2006; Lindsey & Fialko, 2013; Lundgren et al., 2009) and is needed to properly assess seismic hazard. For instance, Lindsey and Fialko (2013) explore several physical models with distinct fault geometries or spatial heterogeneities in the crustal elastic properties to estimate the slip rate on each of these faults based on the inversion of GPS and InSAR surface velocities. The ambiguity between those models comes from the very similar resulting surface velocity field. However, these models predict larger differences in surface strain rates than in velocities and could be better distinguished by looking at the fit to the second invariant I_2, for instance. This requires uncertainties on I_2 to be correctly estimated, as done here and shown in Figure 10b.

The Bayesian method developed in this study thus allows to identify creeping segments from locking segments and potentially active faults during the interseismic period without a priori constraints on the structure of deformation. It is also to note that it jointly retrieves the velocity field and its derivatives in areas of large strain rates such as the San Andreas fault system, but also in areas of lower deformation rates such as the Wasatch mountains experiencing a ~20 nstrain/yr extension. It appears robust enough to discuss with confidence second-order features of the strain rate tensor that could be meaningful in well-resolved areas. For instance, the surface strain pattern above an active locked fault can show some level of asymmetry depending on the rheology and lithology contrast on either side of the fault (Chéry, 2008; Fialko, 2006; Jolivet et al., 2008; Le Pichon et al., 2005). The posterior distribution for velocity or second invariant could show whether this asymmetry is required by the data.

Furthermore, having access to the uncertainties associated with the principal strain directions will help comparing deformation over broader spatial scale and discuss more finely how strain is partitioned over active structures and within lithospheric blocks. However, this method is primarily dependent on the density and quality of observations, which remains the limiting factor in such discussions.

6.3. Future Developments

The development of modern geodetic techniques in the last decades (with GNSS continuously recording networks, optical and radar satellite imagery, tiltmeters) has led to the generalization of the production of strain rate maps, based on velocities averaged over several years. These maps have a very broad range of applications, in long-term tectonics (e.g., Flesch & Kreemer, 2010; Kreemer et al., 2003), seismic cycle (e.g., D'Agostino, 2014; Klein et al., 2019; H. Wang et al., 2019), or hydrology (e.g., Silverii et al., 2020). Recently, strain rates have been calculated on much shorter time-spans in order to capture the surface deformation associated with phenomena such as ground water variations (Klein et al., 2019; Silverii et al., 2020), magmatic intrusions (Silverii et al., 2019) or slow-slip events (e.g., Delbridge et al., 2020). Our interpolation method, with its ability to properly account for data errors, could prove useful in these cases where observations are associated with larger than usual uncertainties.

The algorithm presented in this study has been designed for and applied to GNSS horizontal velocity fields. It could also be applied to a variety of interpolation problems in the geosciences, providing correct estimates of uncertainties. For instance, one could easily apply our proposed approach to the interpolation of horizontal coseismic displacements and associated strain tensor. Recently, Barnhart et al. (2020) use high-resolution optical images correlation technique to recover the horizontal coseismic displacement associated with the Ridgecrest earthquake sequence that stroke the East California Shear Zone and Garlock fault in 2019 (Mw 6.4 and Mw 7.1 for the main shocks). Their interpretation of the derived dilatation maps in terms of inelastic deformation in the very near field from the fault is highlighted by Feng and Almeida (2020) since it would have important consequences on our understanding of faults and earthquakes. However, as previously shown, dilatation maps are prone to strong interpolation artifacts and should be carefully interpreted, or built with our artifact-free method.

The next step is therefore to adapt our technique to more continuous pictures of the surface deformation as produced by optical image correlation (e.g., Barnhart et al., 2020; Delorme et al., 2020; Vallage et al., 2015) or InSAR (LOS velocities, e.g., Hussain et al., 2016; H. Wang et al., 2019; Weiss et al., 2020). One difficulty to do so is to properly account for the spatially correlated noise between pixels, fully described by a covariance matrix for InSAR (e.g., Lohman & Simons, 2005). Second, image correlation (when including elevation information), and InSAR can provide the vertical displacement field and the projection of horizontal and vertical velocities in the LOS direction, respectively. Our method should therefore be adapted to jointly interpolate the three components of the velocity field (including the vertical velocities coming from high quality GNSS measurements). The implementation is relatively straightforward and will be added in the future, though it will add computational cost. Including vertical velocities will give us access to the horizontal derivatives of V_z that could help identifying active faults, subsidence and uplift patterns. However, even with this more complete view of the 3D strain rate tensor, this latter will remain incomplete as derivative with respect to the vertical direction will be missing. Note that some attempts to take into account the horizontal gradients of the vertical velocity into a pseudo 3D strain rate tensor have been performed by Mazzotti et al. (2005), Shen and Liu (2020), or Piña-Valdés et al. (2020) and could be similarly conducted within our Bayesian framework in the future.

7. Conclusion

We develop a transdimensional Bayesian method, adapted from seismic imaging (Bodin, Salmon, et al., 2012; Bodin, Sambridge, et al., 2012) to estimate surface strain rates from discrete GNSS horizontal velocity fields. Synthetic tests conducted on an idealized velocity field produced by the interseismic loading of the San Andreas fault zone show that this approach is more robust than a standard B-spline interpolation technique. In particular, it is able to correctly recover the strain rate tensor on a wide range of rates, without need of manually tuned user-defined parameters. The solution is a full probability distribution on model parameters de-

fining the velocity field and its spatial derivatives. We propose several ways to visualize the solution through maps of the mean, median, standard deviation, or maximum probability. We also show fault-perpendicular profiles presenting the full posterior distribution. The probability distribution of principal directions of strain rates can be plotted on wind rose diagrams, allowing for a better comparison with long-term tectonic studies.

We apply our method to the MIDAS velocity data set on the San Andreas and Basin and Range area and find that, while in general agreement with previously published strain rate maps, our results are smoother and artifact free. They allow for more rigorous tectonic interpretation, and help discriminating between creeping and locked fault segments. Our Bayesian inversion method designed to solve this very common interpolation and derivation problem will be applied in future work to continuous images of deformation obtained from InSAR or image correlation, with the possibility of combining all types of data sets together. We hope that the proposed approach will allow to take full profit of multi-scale geodetic measurements and to better include them in probabilistic seismic hazard assessment techniques.

Data Availability Statement

Data sets for this research are available at https://doi.org/10.6084/m9.figshare.14538072 under the CC0 license.

Acknowledgments
This work has been supported by the Programme National de Télédétection Spatiale (PNTS, http://www.insu.cnrs.fr/pnts), grant nPNTS-2019-7. It has been conducted in the frame of the European Union's Horizon2020 research and innovation programme under grant agreement no. 716542. The authors would like to thank Camille Noûs and the open source Generic Mapping Tool software https://www.generic-mapping-tools.org/. The software described in this study is available on request.

References

Altamimi, Z., Métivier, L., Rebischung, P., Rouby, H., & Collilieux, X. (2017). Itrf2014 plate motion model. *Geophysical Journal International*, *209*(3), 1906–1912. https://doi.org/10.1093/gji/ggx136

Altamimi, Z., Rebischung, P., Métivier, L., & Collilieux, X. (2016). Itrf2014: A new release of the international terrestrial reference frame modeling nonlinear station motions. *Journal of Geophysical Research: Solid Earth*, *121*(8), 6109–6131. https://doi.org/10.1002/2016jb013098

Amos, C. B., Audet, P., Hammond, W. C., Bürgmann, R., Johanson, I. A., & Blewitt, G. (2014). Uplift and seismicity driven by groundwater depletion in central California. *Nature*, *509*(7501), 483–486. https://doi.org/10.1038/nature13275

Angelica, C., Bonforte, A., Distefano, G., Serpelloni, E., & Gresta, S. (2013). Seismic potential in Italy from integration and comparison of seismic and geodetic strain rates. *Tectonophysics*, *608*, 996–1006. https://doi.org/10.1016/j.tecto.2013.07.014

Aster, R. C., Borchers, B., & Thurber, C. H. (2018). *Parameter estimation and inverse problems*. Elsevier.

Avouac, J.-P. (2015). From geodetic imaging of seismic and aseismic fault slip to dynamic modeling of the seismic cycle. *Annual Review of Earth and Planetary Sciences*, *43*, 233–271. https://doi.org/10.1146/annurev-earth-060614-105302

Barnhart, W. D., Gold, R. D., & Hollingsworth, J. (2020). Localized fault-zone dilatancy and surface inelasticity of the 2019 Ridgecrest earthquakes. *Nature Geoscience*, *13*(10), 699–704. https://doi.org/10.1038/s41561-020-0628-8

Baxter, S. C., Kedar, S., Parker, J. W., Webb, F. H., Owen, S. E., Sibthorpe, A., & Dong, D. (2011). Limitations of strain estimation techniques from discrete deformation observations. *Geophysical Research Letters*, *38*(1). https://doi.org/10.1029/2010gl046028

Beauval, C., Marinière, J., Yepes, H., Audin, L., Nocquet, J. M., Alvarado, A., et al. (2018). A new seismic hazard model for Ecuador. *Bulletin of the Seismological Society of America*, *108*(3A), 1443–1464. https://doi.org/10.1785/0120170259

Beavan, J., & Haines, J. (2001). Contemporary horizontal velocity and strain rate fields of the Pacific-Australian plate boundary zone through New Zealand. *Journal of Geophysical Research*, *106*(B1), 741–770. https://doi.org/10.1029/2000jb900302

Ben-Zion, Y., Rice, J. R., & Dmowska, R. (1993). Interaction of the San Andreas Fault creeping segment with adjacent great rupture zones and earthquake recurrence at Parkfield. *Journal of Geophysical Research*, *98*(B2), 2135–2144. https://doi.org/10.1029/92jb02154

Bennett, R. A., & Hreinsdóttir, S. (2007). Constraints on vertical crustal motion for long baselines in the central Mediterranean region using continuous GPS. *Earth and Planetary Science Letters*, *257*(3–4), 419–434. https://doi.org/10.1016/j.epsl.2007.03.008

Bennett, R. A., Wernicke, B., Niemi, N., Friedrich, A., & Davis, J. (2003). Contemporary strain rates in the northern Basin and Range province from GPS data. *Tectonics*, *22*(2). https://doi.org/10.1029/2001tc001355

Benoist, C., Collilieux, X., Rebischung, P., Altamimi, Z., Jamet, O., Métivier, L., et al. (2020). Accounting for spatiotemporal correlations of GNSS coordinate time series to estimate station velocities. *Journal of Geodynamics*, *135*, 101693. https://doi.org/10.1016/j.jog.2020.101693

Blewitt, G., Hammond, W. C., & Kreemer, C. (2009). *Geodetic observation of contemporary deformation in the northern Walker Lane: 1. Semipermanent GPS strategy* (Geological Society of America Special Paper, pp. 1–15).

Blewitt, G., Hammond, W. C., & Kreemer, C. (2018). Harnessing the GPS data explosion for interdisciplinary science. *Eos, Transactions, American Geophysical Union*, *99*, 1–2. https://doi.org/10.1029/2018eo104623

Blewitt, G., Kreemer, C., Hammond, W. C., & Gazeaux, J. (2016). Midas robust trend estimator for accurate GPS station velocities without step detection. *Journal of Geophysical Research: Solid Earth*, *121*(3), 2054–2068. https://doi.org/10.1002/2015jb012552

Bodin, T., Salmon, M., Kennett, B., & Sambridge, M. (2012). Probabilistic surface reconstruction from multiple data sets: An example for the Australian Moho. *Journal of Geophysical Research*, *117*(B10). https://doi.org/10.1029/2012jb009547

Bodin, T., & Sambridge, M. (2009). Seismic tomography with the reversible jump algorithm. *Geophysical Journal International*, *178*(3), 1411–1436. https://doi.org/10.1111/j.1365-246x.2009.04226.x

Bodin, T., Sambridge, M., Rawlinson, N., & Arroucau, P. (2012). Transdimensional tomography with unknown data noise. *Geophysical Journal International*, *189*(3), 1536–1556. https://doi.org/10.1111/j.1365-246x.2012.05414.x

Brooks, S., Gelman, A., Jones, G., & Meng, X.-L. (2011). *Handbook of Markov chain Monte Carlo*. CRC press.

Bürgmann, R., & Thatcher, W. (2013). Space geodesy: A revolution in crustal deformation measurements of tectonic processes. *Geological Society of America Special Paper*, *500*, 397–430.

Cai, J., Wang, J., Wu, J., Hu, C., Grafarend, E., & Chen, J. (2008). Horizontal deformation rate analysis based on multiepoch GPS measurements in shanghai. *Journal of Surveying Engineering*, *134*(4), 132–137. https://doi.org/10.1061/(asce)0733-9453(2008)134:4(132)

Chaussard, E., Milillo, P., Bürgmann, R., Perissin, D., Fielding, E. J., & Baker, B. (2017). Remote sensing of ground deformation for monitoring groundwater management practices: Application to the Santa Clara Valley during the 2012-2015 California drought. *Journal of Geophysical Research: Solid Earth*, *122*(10), 8566–8582. https://doi.org/10.1002/2017jb014676

Chéry, J. (2008). Geodetic strain across the San Andreas Fault reflects elastic plate thickness variations (rather than fault slip rate). *Earth and Planetary Science Letters*, *269*(3–4), 352–365. https://doi.org/10.1016/j.epsl.2008.01.046

Chlieh, M., Avouac, J.-P., Sieh, K., Natawidjaja, D. H., & Galetzka, J. (2008). Heterogeneous coupling of the Sumatran megathrust constrained by geodetic and paleogeodetic measurements. *Journal of Geophysical Research*, *113*(B5). https://doi.org/10.1029/2007jb004981

Choblet, G., Husson, L., & Bodin, T. (2014). Probabilistic surface reconstruction of coastal sea level rise during the twentieth century. *Journal of Geophysical Research: Solid Earth*, *119*(12), 9206–9236. https://doi.org/10.1002/2014jb011639

Chousianitis, K., Ganas, A., & Evangelidis, C. P. (2015). Strain and rotation rate patterns of mainland Greece from continuous GPS data and comparison between seismic and geodetic moment release. *Journal of Geophysical Research: Solid Earth*, *120*(5), 3909–3931. https://doi.org/10.1002/2014jb011762

Copley, A. (2008). Kinematics and dynamics of the southeastern margin of the Tibetan plateau. *Geophysical Journal International*, *174*(3), 1081–1100. https://doi.org/10.1111/j.1365-246x.2008.03853.x

D'Agostino, N. (2014). Complete seismic release of tectonic strain and earthquake recurrence in the Apennines (Italy). *Geophysical Research Letters*, *41*(4), 1155–1162.

D'Agostino, N., England, P., Hunstad, I., & Selvaggi, G. (2014). Gravitational potential energy and active deformation in the Apennines. *Earth and Planetary Science Letters*, *397*, 121–132.

Delbridge, B. G., Carmichael, J. D., Nadeau, R. M., Shelly, D. R., & Bürgmann, R. (2020). Geodetic measurements of slow-slip events southeast of Parkfield, CA. *Journal of Geophysical Research: Solid Earth*, *125*(5), e2019JB019059. https://doi.org/10.1029/2019jb019059

Delorme, A., Grandin, R., Klinger, Y., Pierrot-Deseilligny, M., Feuillet, N., Jacques, E., et al. (2020). Complex deformation at shallow depth during the 30 October 2016 Mw6. 5 Norcia earthquake: Interference between tectonic and gravity processes? *Tectonics*, *39*(2), e2019TC005596. https://doi.org/10.1029/2019tc005596

Dong, D., Fang, P., Bock, Y., Webb, F., Prawirodirdjo, L., Kedar, S., & Jamason, P. (2006). Spatiotemporal filtering using principal component analysis and Karhunen-Loeve expansion approaches for regional GPS network analysis. *Journal of Geophysical Research*, *111*(B3). https://doi.org/10.1029/2005jb003806

Elliott, J., Walters, R., & Wright, T. (2016). The role of space-based observation in understanding and responding to active tectonics and earthquakes. *Nature Communications*, *7*(1), 1–16. https://doi.org/10.1038/ncomms13844

England, P., Houseman, G., & Nocquet, J.-M. (2016). Constraints from GPS measurements on the dynamics of deformation in Anatolia and the Aegean. *Journal of Geophysical Research: Solid Earth*, *121*(12), 8888–8916. https://doi.org/10.1002/2016jb013382

England, P., & Molnar, P. (1997). Active deformation of Asia: From kinematics to dynamics. *Science*, *278*(5338), 647–650. https://doi.org/10.1126/science.278.5338.647

Farolfi, G., & Del Ventisette, C. (2017). Strain rates in the alpine Mediterranean region: Insights from advanced techniques of data processing. *GPS Solutions*, *21*(3), 1027–1036. https://doi.org/10.1007/s10291-016-0588-z

Feng, W., & Almeida, R. V. (2020). Inelastic earthquake damage. *Nature Geoscience*, *13*(10), 661–662. https://doi.org/10.1038/s41561-020-0642-x

Fialko, Y. (2006). Interseismic strain accumulation and the earthquake potential on the southern San Andreas fault system. *Nature*, *441*(7096), 968–971. https://doi.org/10.1038/nature04797

Flesch, L. M., & Kreemer, C. (2010). Gravitational potential energy and regional stress and strain rate fields for continental plateaus: Examples from the central Andes and Colorado Plateau. *Tectonophysics*, *482*(1–4), 182–192. https://doi.org/10.1016/j.tecto.2009.07.014

Frank, F. (1966). Deduction of earth strains from survey data. *Bulletin of the Seismological Society of America*, *56*(1), 35–42.

Freymueller, J. T., Murray, M. H., Segall, P., & Castillo, D. (1999). Kinematics of the Pacific-North America plate boundary zone, Northern California. *Journal of Geophysical Research*, *104*(B4), 7419–7441. https://doi.org/10.1029/1998jb900118

Gan, W., Zhang, P., Shen, Z.-K., Niu, Z., Wang, M., Wan, Y., et al. (2007). Present-day crustal motion within the Tibetan Plateau inferred from GPS measurements. *Journal of Geophysical Research*, *112*(B8). https://doi.org/10.1029/2005jb004120

Gerstenberger, M. C., Marzocchi, W., Allen, T., Pagani, M., Adams, J., Danciu, L., et al. (2020). Probabilistic seismic hazard analysis at regional and national scales: State of the art and future challenges. *Reviews of Geophysics*, *58*(2), e2019RG000653. https://doi.org/10.1029/2019rg000653

Geyer, C. J. (1992). Practical Markov chain Monte Carlo. *Statistical Science*, 473–483.

Gouveia, W. P., & Scales, J. A. (1998). Bayesian seismic waveform inversion: Parameter estimation and uncertainty analysis. *Journal of Geophysical Research*, *103*(B2), 2759–2779. https://doi.org/10.1029/97jb02933

Green, P. J. (1995). Reversible jump Markov chain Monte Carlo computation and Bayesian model determination. *Biometrika*, *82*(4), 711–732. https://doi.org/10.1093/biomet/82.4.711

Green, P. J. (2003). *Trans-dimensional Markov chain Monte Carlo* (Oxford Statistical Science Series, pp. 179–198).

Hackl, M., Malservisi, R., & Wdowinski, S. (2009). Strain rate patterns from dense GPS networks. *Natural Hazards and Earth System Sciences*, *9*, 1177–1187. https://doi.org/10.5194/nhess-9-1177-2009

Haines, A. J., & Holt, W. E. (1993). A procedure for obtaining the complete horizontal motions within zones of distributed deformation from the inversion of strain rate data. *Journal of Geophysical Research*, *98*(B7), 12057–12082. https://doi.org/10.1029/93jb00892

Hammond, W. C., Blewitt, G., & Kreemer, C. (2016). GPS imaging of vertical land motion in California and Nevada: Implications for Sierra Nevada uplift. *Journal of Geophysical Research: Solid Earth*, *121*(10), 7681–7703. https://doi.org/10.1002/2016jb013458

Hammond, W. C., Kreemer, C., Zaliapin, I., & Blewitt, G. (2019). Drought-triggered magmatic inflation, crustal strain, and seismicity near the Long Valley Caldera, Central Walker Lane. *Journal of Geophysical Research: Solid Earth*, *124*(6), 6072–6091. https://doi.org/10.1029/2019jb017354

Hastings, W. K. (1970). Monte Carlo sampling methods using Markov chains and their applications. *Biometrika*, *57*(1), 97–109.

Hawkins, R., Bodin, T., Sambridge, M., Choblet, G., & Husson, L. (2019). Trans-dimensional surface reconstruction with different classes of parameterization. *Geochemistry, Geophysics, Geosystems*, *20*(1), 505–529. https://doi.org/10.1029/2018gc008022

Hawkins, R., Husson, L., Choblet, G., Bodin, T., & Pfeffer, J. (2019). Virtual tide gauges for predicting relative sea level rise. *Journal of Geophysical Research: Solid Earth*, *124*(12), 13367–13391. https://doi.org/10.1029/2019jb017943

Herring, T. A., Melbourne, T. I., Murray, M. H., Floyd, M. A., Szeliga, W. M., King, R. W., et al. (2016). Plate boundary observatory and related networks: GPS data analysis methods and geodetic products. *Reviews of Geophysics*, *54*(4), 759–808. https://doi.org/10.1002/2016rg000529

Holt, W. E., Chamot-Rooke, N., Le Pichon, X., Haines, A. J., Shen-Tu, B., & Ren, J. (2000). Velocity field in Asia inferred from quaternary fault slip rates and global positioning system observations. *Journal of Geophysical Research*, *105*(B8), 19185–19209. https://doi.org/10.1029/2000jb900045

Hudnut, K. W., Bock, Y., Galetzka, J. E., Webb, F. H., & Young, W. H. (2001). *The southern California integrated GPS network (SCIGN)* (pp. 19–22). Paper presented at the 10th FIG International Symposium on Deformation Measurements.

Hussain, E., Hooper, A., Wright, T. J., Walters, R. J., & Bekaert, D. P. S. (2016). Interseismic strain accumulation across the central north Anatolian fault from iteratively unwrapped INSAR measurements. *Journal of Geophysical Research: Solid Earth*, *121*(12), 9000–9019. https://doi.org/10.1002/2016jb013108

Husson, L., Bodin, T., Spada, G., Choblet, G., & Kreemer, C. (2018). Bayesian surface reconstruction of geodetic uplift rates: Mapping the global fingerprint of glacial isostatic adjustment. *Journal of Geodynamics*, *122*, 25–40. https://doi.org/10.1016/j.jog.2018.10.002

Isacks, B., Oliver, J., & Sykes, L. R. (1968). Seismology and the new global tectonics. *Journal of Geophysical Research*, *73*(18), 5855–5899. https://doi.org/10.1029/jb073i018p05855

Jolivet, R., Cattin, R., Chamot-Rooke, N., Lasserre, C., & Peltzer, G. (2008). Thin-plate modeling of interseismic deformation and asymmetry across the Altyn Tagh Fault Zone. *Geophysical Research Letters*, *35*(2). https://doi.org/10.1029/2007gl031511

Jolivet, R., Simons, M., Agram, P. S., Duputel, Z., & Shen, Z.-K. (2015). Aseismic slip and seismogenic coupling along the central San Andreas Fault. *Geophysical Research Letters*, *42*(2), 297–306. https://doi.org/10.1002/2014gl062222

Kaneko, Y., Avouac, J.-P., & Lapusta, N. (2010). Towards inferring earthquake patterns from geodetic observations of interseismic coupling. *Nature Geoscience*, *3*(5), 363–369. https://doi.org/10.1038/ngeo843

Kim, J., Bahadori, A., & Holt, W. E. (2021). Crustal strain patterns associated with normal, drought, and heavy precipitation years in California. *Journal of Geophysical Research: Solid Earth*, *126*(1), e2020JB019560. https://doi.org/10.1029/2020jb019560

Klein, E., Bock, Y., Xu, X., Sandwell, D. T., Golriz, D., Fang, P., & Su, L. (2019). Transient deformation in California from two decades of GPS displacements: Implications for a three-dimensional kinematic reference frame. *Journal of Geophysical Research: Solid Earth*, *124*(11), 12189–12223. https://doi.org/10.1029/2018jb017201

Kostrov, V. (1974). Seismic moment and energy of earthquakes, and seismic flow of rock. *Izvestiya, Physics of the Solid Earth*, *1*, 23–44.

Kreemer, C., Blewitt, G., & Klein, E. C. (2014). A geodetic plate motion and global strain rate model. *Geochemistry, Geophysics, Geosystems*, *15*(10), 3849–3889. https://doi.org/10.1002/2014gc005407

Kreemer, C., & Hammond, W. C. (2007). Geodetic constraints on areal changes in the Pacific-North America plate boundary zone: What controls Basin and Range extension? *Geology*, *35*(10), 943–946. https://doi.org/10.1130/g23868a.1

Kreemer, C., Hammond, W. C., & Blewitt, G. (2018). A robust estimation of the 3-D intraplate deformation of the North American plate from GPS. *Journal of Geophysical Research: Solid Earth*, *123*(5), 4388–4412. https://doi.org/10.1029/2017jb015257

Kreemer, C., Hammond, W. C., Blewitt, G., Holland, A. A., & Bennett, R. A. (2012). *A geodetic strain rate model for the Pacific-North American plate boundary, Western United States* (p. 6785). EGUGA.

Kreemer, C., Holt, W. E., & Haines, A. J. (2003). An integrated global model of present-day plate motions and plate boundary deformation. *Geophysical Journal International*, *154*(1), 8–34. https://doi.org/10.1046/j.1365-246x.2003.01917.x

Le Pichon, X. (1968). Sea-floor spreading and continental drift. *Journal of Geophysical Research*, *73*(12), 3661–3697. https://doi.org/10.1029/jb073i012p03661

Le Pichon, X., Kreemer, C., & Chamot-Rooke, N. (2005). Asymmetry in elastic properties and the evolution of large continental strike-slip faults. *Journal of Geophysical Research*, *110*(B3). https://doi.org/10.1029/2004jb003343

Lindsey, E. O., & Fialko, Y. (2013). Geodetic slip rates in the southern San Andreas Fault system: Effects of elastic heterogeneity and fault geometry. *Journal of Geophysical Research: Solid Earth*, *118*(2), 689–697. https://doi.org/10.1029/2012jb009358

Lohman, R. B., & Simons, M. (2005). Some thoughts on the use of INSAR data to constrain models of surface deformation: Noise structure and data downsampling. *Geochemistry, Geophysics, Geosystems*, *6*(1). https://doi.org/10.1029/2004gc000841

Lundgren, P., Hetland, E. A., Liu, Z., & Fielding, E. J. (2009). Southern San Andreas-San Jacinto Fault System slip rates estimated from earthquake cycle models constrained by GPS and interferometric synthetic aperture radar observations. *Journal of Geophysical Research*, *114*(B2). https://doi.org/10.1029/2008jb005996

Machette, M. N., Personius, S. F., Nelson, A. R., Schwartz, D. P., & Lund, W. R. (1991). The Wasatch fault zone, Utah-segmentation and history of Holocene earthquakes. *Journal of Structural Geology*, *13*(2), 137–149. https://doi.org/10.1016/0191-8141(91)90062-n

Marshall, G. A., Langbein, J., Stein, R. S., Lisowski, M., & Svarc, J. (1997). Inflation of Long Valley Caldera, California, Basin and Range Strain, and possible mono craters dike opening from 1990-94 GPS surveys. *Geophysical Research Letters*, *24*(9), 1003–1006. https://doi.org/10.1029/97gl00885

Masson, C., Mazzotti, S., Vernant, P., & Doerflinger, E. (2019). Extracting small deformation beyond individual station precision from dense global navigation satellite system (GNSS) networks in France and Western Europe. *Solid Earth*, *10*(6), 1905–1920. https://doi.org/10.5194/se-10-1905-2019

Mathey, M., Walpersdorf, A., Sue, C., Baize, S., & Deprez, A. (2020). Seismogenic potential of the high durance fault constrained by 20 yr of GNSS measurements in the Western European Alps. *Geophysical Journal International*, *222*(3), 2136–2146. https://doi.org/10.1093/gji/ggaa292

Mazzotti, S., Déprez, A., Henrion, E., Masson, C., Masson, F., Menut, J.-L., et al. (2020). *Comparative analysis of synthetic GNSS time series-bias and precision of velocity estimations* (Unpublished Doctoral Dissertation). RESIF.

Mazzotti, S., James, T. S., Henton, J., & Adams, J. (2005). GPS crustal strain, postglacial rebound, and seismic hazard in eastern North America: The Saint Lawrence Valley example. *Journal of Geophysical Research*, *110*(B11). https://doi.org/10.1029/2004jb003590

Mazzotti, S., Leonard, L., Cassidy, J., Rogers, G., & Halchuk, S. (2011). Seismic hazard in western Canada from GPS strain rates versus earthquake catalog. *Journal of Geophysical Research*, *116*(B12). https://doi.org/10.1029/2011jb008213

McCaffrey, R. (2005). Block kinematics of the Pacific–North America plate boundary in the southwestern United States from inversion of GPS, seismological, and geologic data. *Journal of Geophysical Research*, *110*(B7). https://doi.org/10.1029/2004jb003307

McCaffrey, R., King, R. W., Payne, S. J., & Lancaster, M. (2013). Active tectonics of northwestern U.S. inferred from GPS-derived surface velocities. *Journal of Geophysical Research: Solid Earth*, *118*(2), 709–723. https://doi.org/10.1029/2012jb009473

Métois, M., D'Agostino, N., Avallone, A., Chamot-Rooke, N., Rabaute, A., Duni, L., et al. (2015). Insights on continental collisional processes from GPS data: Dynamics of the peri-Adriatic belts. *Journal of Geophysical Research: Solid Earth*, *120*(12), 8701–8719. https://doi.org/10.1002/2015jb012023

Métois, M., Vigny, C., & Socquet, A. (2016). Interseismic coupling, megathrust earthquakes and seismic swarms along the Chilean subduction zone (38°-18°S). *Pure and Applied Geophysics*, *173*(5), 1431–1449. https://doi.org/10.1007/s00024-016-1280-5

Metropolis, N., Rosenbluth, A. W., Rosenbluth, M. N., Teller, A. H., & Teller, E. (1953). Equation of state calculations by fast computing machines. *The Journal of Chemical Physics*, *21*(6), 1087–1092. https://doi.org/10.1063/1.1699114

Milliner, C., & Donnellan, A. (2020). Using daily observations from planet labs satellite imagery to separate the surface deformation between the 4 July Mw 6.4 foreshock and 5 July Mw 7.1 mainshock during the 2019 Ridgecrest Earthquake sequence. *Seismological Research Letters*, *91*(4), 1986–1997. https://doi.org/10.1785/0220190271

Morgan, W. J. (1968). Rises, trenches, great faults, and crustal blocks. *Journal of Geophysical Research*, *73*(6), 1959–1982. https://doi.org/10.1029/jb073i006p01959

Murray, J., & Langbein, J. (2006). Slip on the San Andreas Fault at Parkfield, California, over two earthquake cycles, and the implications for seismic hazard. *Bulletin of the Seismological Society of America*, *96*(4B), S283–S303. https://doi.org/10.1785/0120050820

Niemi, N. A., Wernicke, B. P., Friedrich, A. M., Simons, M., Bennett, R. A., & Davis, J. L. (2004). Bargen continuous GPS data across the eastern basin and range province, and implications for fault system dynamics. *Geophysical Journal International*, *159*(3), 842–862. https://doi.org/10.1111/j.1365-246x.2004.02454.x

Okada, Y. (1985). Surface deformation due to shear and tensile faults in a half-space. *Bulletin of the Seismological Society of America*, *75*(4), 1135–1154.

Palano, M., Imprescia, P., Agnon, A., & Gresta, S. (2018). An improved evaluation of the seismic/geodetic deformation-rate ratio for the Zagros fold-and-thrust collisional belt. *Geophysical Journal International*, *213*(1), 194–209. https://doi.org/10.1093/gji/ggx524

Pancha, A., Anderson, J. G., & Kreemer, C. (2006). Comparison of seismic and geodetic scalar moment rates across the basin and range province. *Bulletin of the Seismological Society of America*, *96*(1), 11–32. https://doi.org/10.1785/0120040166

Parsons, T. (2006). Tectonic stressing in California modeled from GPS observations. *Journal of Geophysical Research*, *111*(B3). https://doi.org/10.1029/2005jb003946

Peltzer, G., Crampé, F., Hensley, S., & Rosen, P. (2001). Transient strain accumulation and fault interaction in the eastern California shear zone. *Geology*, *29*(11), 975–978. https://doi.org/10.1130/0091-7613(2001)029<0975:tsaafi>2.0.co;2

Pérouse, E., Chamot-Rooke, N., Rabaute, A., Briole, P., Jouanne, F., Georgiev, I., & Dimitrov, D. (2012). Bridging onshore and offshore present-day kinematics of central and eastern Mediterranean: Implications for crustal dynamics and mantle flow. *Geochemistry, Geophysics, Geosystems*, *13*(9). https://doi.org/10.1029/2012gc004289

Pérouse, E., & Wernicke, B. P. (2017). Spatiotemporal evolution of fault slip rates in deforming continents: The case of the great basin region, northern basin and range province. *Geosphere*, *13*(1), 112–135. https://doi.org/10.1130/ges01295.1

Piña-Valdés, J., Socquet, A., Beauval, C., Bard, P.-Y., Doin, M.-P., & Shen, Z. (2020). *Toward the development of earthquake recurrence models from 3D GNSS velocity field in Europe* (p. 19808). Paper presented in EGU General Assembly Conference Abstracts.

Quaternary Fault and Fold Database. (2019).*U.S. geological survey and New Mexico bureau of mines and mineral resources, quaternary fault and fold database for the United States*. Retrieved from https://www.usgs.gov/natural-hazards/earthquake-hazards/faults

Rolandone, F., Bürgmann, R., Agnew, D., Johanson, I., Templeton, D., d'Alessio, M., et al. (2008). Aseismic slip and fault-normal strain along the central creeping section of the San Andreas Fault. *Geophysical Research Letters*, *35*(14). https://doi.org/10.1029/2008gl034437

Sagiya, T., Miyazaki, S. i., & Tada, T. (2000). Continuous GPS array and present-day crustal deformation of Japan. *Pure and Applied Geophysics*, *157*(11–12), 2303–2322. https://doi.org/10.1007/978-3-0348-7695-7_26

Sambridge, M., Bodin, T., Gallagher, K., & Tkalčić, H. (2013). Transdimensional inference in the geosciences. *Philosophical Transactions of the Royal Society A: Mathematical, Physical & Engineering Sciences*, *371*(1984), 20110547. https://doi.org/10.1098/rsta.2011.0547

Sambridge, M., & Mosegaard, K. (2002). Monte Carlo methods in geophysical inverse problems. *Reviews of Geophysics*, *40*(3), 3–1. https://doi.org/10.1029/2000rg000089

Sandwell, D., Becker, T., Bird, P., Freed, A., Hackl, M., Holt, W., et al. (2010). Comparison of 16 strain-rate maps of southern California. *SCEC Presentation*, *1*(5).

Santamaría-Gómez, A., Bouin, M.-N., Collilieux, X., & Wöppelmann, G. (2011). Correlated errors in GPS position time series: Implications for velocity estimates. *Journal of Geophysical Research*, *116*(B1). https://doi.org/10.1029/2010jb007701

Savage, J. (1983). A dislocation model of strain accumulation and release at a subduction zone. *Journal of Geophysical Research*, *88*(3), 4984–4996. https://doi.org/10.1029/jb088ib06p04984

Savage, J., & Burford, R. (1970). Accumulation of tectonic strain in California. *Bulletin of the Seismological Society of America*, *60*(6), 1877–1896.

Shen, Z.-K., Jackson, D. D., Feng, Y., Cline, M., Kim, M., Fang, P., & Bock, Y. (1994). Postseismic deformation following the landers earthquake, California, 28 June 1992. *Bulletin of the Seismological Society of America*, *84*(3), 780–791.

Shen, Z.-K., Jackson, D. D., & Ge, B. X. (1996). Crustal deformation across and beyond the Los Angeles basin from geodetic measurements. *Journal of Geophysical Research*, *101*(B12), 27957–27980. https://doi.org/10.1029/96jb02544

Shen, Z.-K., Jackson, D. D., & Kagan, Y. Y. (2007). Implications of geodetic strain rate for future earthquakes, with a five-year forecast of m5 earthquakes in southern California. *Seismological Research Letters*, *78*(1), 116–120. https://doi.org/10.1785/gssrl.78.1.116

Shen, Z.-K., & Liu, Z. (2020). Integration of GPS and INSAR data for resolving 3-dimensional crustal deformation. *Earth and Space Science*, *7*(4), e2019EA001036. https://doi.org/10.1029/2019ea001036

Shen, Z.-K., Wang, M., Zeng, Y., & Wang, F. (2015). Optimal interpolation of spatially discretized geodetic data. *Bulletin of the Seismological Society of America*, *105*(4), 2117–2127. https://doi.org/10.1785/0120140247

Silverii, F., D'Agostino, N., Borsa, A. A., Calcaterra, S., Gambino, P., Giuliani, R., & Mattone, M. (2019). Transient crustal deformation from karst aquifers hydrology in the Apennines (Italy). *Earth and Planetary Science Letters*, *506*, 23–37. https://doi.org/10.1016/j.epsl.2018.10.019

Silverii, F., Montgomery-Brown, E., Borsa, A., & Barbour, A. (2020). Hydrologically induced deformation in long valley caldera and adjacent Sierra Nevada. *Journal of Geophysical Research: Solid Earth*, *125*(5). https://doi.org/10.1029/2020jb019495

Simons, M., Minson, S. E., Sladen, A., Ortega, F., Jiang, J., Owen, S. E., et al. (2011). The 2011 magnitude 9.0 Tohoku-Oki earthquake: Mosaicking the megathrust from seconds to centuries. *Science*, *332*(6036), 1421–1425. https://doi.org/10.1126/science.1206731

Smith, W. H. F., & Wessel, P. (1990). Gridding with continuous curvature splines in tension. *Geophysics*, *55*(3), 293–305. https://doi.org/10.1190/1.1442837

Snay, R. A., Cline, M. W., & Timmerman, E. L. (1983). Regional deformation of the earth model for the San Diego region, California. *Journal of Geophysical Research*, *88*(B6), 5009–5024. https://doi.org/10.1029/jb088ib06p05009

Spakman, W., & Nyst, M. C. J. (2002). Inversion of relative motion data for estimates of the velocity gradient field and fault slip. *Earth and Planetary Science Letters*, *203*(1), 577–591. https://doi.org/10.1016/s0012-821x(02)00844-0

Tarantola, A. (2005). *Inverse problem theory and methods for model parameter estimation*. SIAM. https://doi.org/10.1137/1.9780898717921
Thatcher, W. (2009). How the continents deform: The evidence from tectonic geodesy. *Annual Review of Earth and Planetary Sciences*, *37*. https://doi.org/10.1146/annurev.earth.031208.100035
Titus, S. J., Dyson, M., DeMets, C., Tikoff, B., Rolandone, F., & Bürgmann, R. (2011). Geologic versus geodetic deformation adjacent to the San Andreas Fault, Central California. *Bulletin*, *123*(5–6), 794–820. https://doi.org/10.1130/b30150.1
Vallage, A., Klinger, Y., Grandin, R., Bhat, H., & Pierrot-Deseilligny, M. (2015). Inelastic surface deformation during the 2013 mw 7.7 Balochistan, Pakistan, earthquake. *Geology*, *43*(12), 1079–1082.
Vergnolle, M., Calais, E., & Dong, L. (2007). Dynamics of continental deformation in Asia. *Journal of Geophysical Research*, *112*(B11). https://doi.org/10.1029/2006jb004807
Wang, H., Wright, T. J., Liu-Zeng, J., & Peng, L. (2019). Strain rate distribution in south-central Tibet from two decades of InSAR and GPS. *Geophysical Research Letters*, *46*(10), 5170–5179. https://doi.org/10.1029/2019gl081916
Wang, K., & Bürgmann, R. (2020). Co- and early postseismic deformation due to the 2019 Ridgecrest earthquake sequence constrained by Sentinel-1 and COSMO-SkyMed SAR Data. *Seismological Research Letters*, *91*(4), 1998–2009. https://doi.org/10.1785/0220190299
Ward, S. N. (1998). On the consistency of earthquake moment rates, geological fault data, and space geodetic strain: The United States. *Geophysical Journal International*, *134*(1), 172–186. https://doi.org/10.1046/j.1365-246x.1998.00556.x
Wdowinski, S., Bock, Y., Zhang, J., Fang, P., & Genrich, J. (1997). Southern California permanent GPS geodetic array: Spatial filtering of daily positions for estimating coseismic and postseismic displacements induced by the 1992 landers earthquake. *Journal of Geophysical Research*, *102*(B8), 18057–18070. https://doi.org/10.1029/97jb01378
Weiss, J. R., Walters, R. J., Morishita, Y., Wright, T. J., Lazecky, M., Wang, H., et al. (2020). High-resolution surface velocities and strain for Anatolia from sentinel-1 INSAR and GNSS data. *Geophysical Research Letters*, *47*(17), e2020GL087376. https://doi.org/10.1029/2020gl087376
Wesnousky, S. G., Bormann, J. M., Kreemer, C., Hammond, W. C., & Brune, J. N. (2012). Neotectonics, geodesy, and seismic hazard in the northern walker lane of western North America: Thirty kilometers of crustal shear and no strike-slip? *Earth and Planetary Science Letters*, *329–330*, 133–140. https://doi.org/10.1016/j.epsl.2012.02.018
Wessel, P., & Becker, J. M. (2008). Interpolation using a generalized Green's function for a spherical surface spline in tension. *Geophysical Journal International*, *174*(1), 21–28. https://doi.org/10.1111/j.1365-246x.2008.03829.x
Wessel, P., & Bercovici, D. (1998). Interpolation with splines in tension: A green's function approach. *Mathematical Geology*, *30*(1), 77–93. https://doi.org/10.1023/a:1021713421882
Wessel, P., Luis, J. F., Uieda, L., Scharroo, R., Wobbe, F., Smith, W. H. F., & Tian, D. (2019). The generic mapping tools version 6. *Geochemistry, Geophysics, Geosystems*, *20*(11), 5556–5564. https://doi.org/10.1029/2019gc008515
Williams, S. D., Bock, Y., Fang, P., Jamason, P., Nikolaidis, R. M., Prawirodirdjo, L., et al. (2004). Error analysis of continuous GPS position time series. *Journal of Geophysical Research*, *109*(B3). https://doi.org/10.1029/2003jb002741